Subcontractor Report

Subcontract Report

Novel Capacitance Measurements in Copper Indium Gallium Diselenide Alloys

Final Subcontract Report
1 July 1999–31 August 2003

D.C. Johnson
University of Oregon
Eugene, Oregon

NREL

Novel Capacitance Measurements in Copper Indium Gallium Diselenide Alloys

Final Subcontract Report
1 July 1999–31 August 2003

D.C. Johnson
University of Oregon
Eugene, Oregon

NREL

PREFACE

This Final Technical Progress Report covers the work performed at the University of Oregon for the period July 1, 1999 to August 31, 2003 under NREL Subcontract Number XAD-9-18668-15. The following personnel participated in this research program:

NAME	TITLE	WORK PERFORMED
David C. Johnson	Professor, Principal Investigator	Program Manager
J. David Cohen	Professor	Supervised sample characterization studies by capacitance methods
Jennifer T. Heath	Research Assistant	Characterization of CIGS and CIAS samples by photocapacitance spectroscopy, DLCP, and related methods.
John Thompson	Research Assistant	Synthesis of CIS and CIGS samples by elementally modulated reactants

TABLE OF CONTENTS

LIST OF ILLUSTRATIONS

Page

LIST OF TABLES

EXECUTIVE SUMMARY

The work carried out under NREL Subcontract Number XAD-9-18668-15 has concentrated on two areas of study. For the first area, we applied a new synthetic method to the production of CIGS alloys; namely, the modulated elemental reactant method. To form CIGS by this method, alternating layers Cu:In:Se and Cu:Ga:Se composites, each less than 100Å thick, were evaporated in sequence and then annealed at low temperature. The formation of the desired CIGS chalcopyrite phase was monitored by X-ray diffraction as the temperature was raised. The desired phase was achieved once an annealing temperature of 400°C was reached. By using multiple repetitions of the reactant layers, CGS, CIS, and CIGS samples up to 1 micron in thickness were produced. Several of these thicker samples were deposited on Mo coated glass and were recently completed as photovoltaic devices by the deposition of CdS and ZnO contacting layers courtesy of Bill Shafarman at the Institute of Energy Conversion (IEC). The best of these test devices achieved a conversion efficiency of only 2.5%; however, we hope that further and more rapid improvement will be possible once we have carried out a detailed characterization of their electronic properties.

The second focus of this Subcontract supported work has been to test and develop junction capacitance methods to better understand the electronic properties in CIGS material and establish a relationship of those properties to specific device performance parameters. The primary methods that were employed under this Subcontract were the transient photocapacitance (TPC) spectroscopy and the drive-level capacitance profiling (DLCP) method. For these characterization studies we relied on CIGS samples obtained from outside sources, primarily from IEC. The TPC spectra we obtained revealed a deep defect band centered about 0.8 eV from the top of the valence band, and also an exponential tail of states into the gap. The deep defect band was found to be present both in polycrystalline CIGS as well as a single crystal epitaxial sample device obtained from the University of Illinois. We found that the 0.8 eV optical transition energy remained constant independent of changes in the Ga fraction. This indicates that the defect lies much closer to midgap as the Ga fraction is increased and is thus more likely to become an important recombination center in the higher Ga fraction alloys. Among the full set of 30at.% Ga fraction CIGS samples devices supplied by IEC, we found that the poorer efficiency devices had lower minority carrier collection and we also found a surprisingly strong correlation that the samples with higher Urbach energies exhibited lower values of the short-circuit current. Using our DLCP measurements we demonstrated that we could obtain superior quantitative estimates of the "deep acceptor level" density and, moreover, the most reliable estimates of the hole carrier densities in such sandwich geometry devices. Numerical modeling was employed to confirm these conclusions, and to point out the detailed relationship and significant differences between the DLCP method with the more familiar techniques of admittance spectroscopy, and normal capacitance voltage profiling.

Finally, we extended our characterization studies to four $CuIn_{1-x}Al_xSe_2$ (CIAS) samples also supplied by IEC. Our photocapacitance and DLCP measurements on these CIAS samples indicated that, for a sample with 13at.% Al (having a bandgap of nearly 1.2eV) the electronic properties were essentially identical to those in CIGS samples with 26at.% Ga. However, for the CIAS samples with 29at.% and higher Al fractions, the electronic properties were found to be relatively poor, as indicated by broader bandtails, poorer minority carrier collection, very nonuniform electronic properties, and generally lower carrier densities.

Novel Capacitance Measurements in Copper Indium Gallium Diselenide Alloys
Final Report
July 1, 1999 – August 31, 2003
Subcontract Number – XAD-9-18668-15
Principal Investigator - David C. Johnson

OBJECTIVE

The objective of this research was to measure the electronic properties of the copper indium/gallium diselenide alloys using several well-developed capacitance techniques appropriate for probing materials with a continuous distribution of semiconducting gap electronic energy states. Optimized CIGS samples, both from our own synthesis approach and from members of the NREL CIGS Team of the Thin-Film Partnership, were characterized.

1.0 TECHNIQUES

Below we briefly describe the techniques used in this project to measure the electrical properties of optimized CIGS samples and the synthesis technique explored to make CIGS samples at Oregon.

1.1 Junction Capacitance Measurements

Junction capacitance measurements were first developed to study and characterize single crystal semiconductors [1, 2]. Although complicated by the continuous distribution and large number of deep levels in the mobility gap, these methods also have been applied successfully to amorphous semiconductors, and in fact, provided the first accurate picture of the density of gap states in hydrogenated amorphous silicon [3,4].

Junction capacitance probes the barrier region formed when joining two materials with different Fermi levels, such as a metal-semiconductor (Schottky) barrier or p+-n semiconductor interface. In an AC junction capacitance measurement on a diode sample, a small modulated voltage of frequency ω is applied to the reversed biased barrier, producing an AC distribution of thermally activated responding charge. Then, if ε and A are the dielectric constant and barrier cross-sectional area, respectively, the measured capacitance is

$$C = \frac{\varepsilon\ A}{<x>} \qquad\qquad [1]$$

where $<x>$ is the first moment of the responding AC charge distribution. The above relation is valid in general, and provides the basis for capacitance profiling techniques. For example, in the case of a single crystal sample in which has one shallow donor or acceptor level, one can

determine the concentration as a function of position using the "profiler's equation" or "CV profile", namely

$$N_{CV} = -\frac{C^3}{\varepsilon\, q\, A^2}\left(\frac{dC}{dV}\right)^{-1} \quad \text{vs.} \quad <x> \qquad [2]$$

where q is the electronic charge. Eqn. [2] allows the crystalline semiconductor's donor concentration to be determined from a capacitance vs. applied voltage (C–V) scan.

Analysis of capacitance data taken on a material with a large and quasi-continuous distribution of semiconductor gap states is more complex. In this situation, the responding AC charge is not localized within the depletion tail (i.e., <x> = W, where W is the depletion width) as assumed in deriving Eqn. [2], but rather the AC charge may be distributed throughout the entire depletion region. In fact, all gap states that can emit a charge carrier to the nearest band edge within the time scale of the bias modulation (angular) frequency ω will contribute to the sample's capacitive response. However, because of the exponential character of carrier emission rates, the measurement frequency imposes a sharp energy cutoff $E_e = k_B T\, \ln(\nu/\omega)$ such that gap states deeper than E_e from the nearest band edge cannot respond to the applied AC voltage. The emission prefactor ν can be determined from the frequency and temperature dependence of the sample's capacitance via Arrenhius plots.

1.2 Drive Level Capacitance Profiling (DLCP)

In the study of amorphous semiconductors, the above observations led to the development of a powerful capacitance characterization technique called "drive-level capacitance profiling" [5]. In this technique, it is noted that a sample's capacitance depends modestly on the amplitude of the applied bias' AC modulation δV ("drive level"). Expanding capacitance in a power series of δV

$$C = C_o + C_1\left(\delta V\right) + C_2\left(\delta V\right)^2 + \dots \qquad [3]$$

then applying Eqn. [1] yields the following relation for the "drive level charge density" N_{DL}

$$N_{DL} = -\frac{C_0^{\,3}}{2q\varepsilon A^2 C_1} = p + \int_{E_{F0}}^{E_V + E_e} g(E,x)\,dE \qquad [4]$$

In the integral E_{F0} is the Fermi energy position and p is the free carrier density in the undepleted film. That is, N_{DL} as determined by C_0 and C_1 is directly related to an integral over the density of states, $g(E,x)$.

By determining N_{DL} for different values of the dc bias, and by varying E_e via different values of temperature or frequency, both a spatial and an energetic profile of the defect density can be obtained. This profile is generally insensitive to the response from states at or near the interface, except for specific values of dc bias which allow the interface states to dynamically respond to the alternating voltage. This last attribute can be particularly useful in distinguishing the interface from bulk response of defects. In contrast, the standard C-V profile is sensitive to all sources of charge change in the film, including the changes in interface charge that occur during

the scan in dc bias, regardless of whether the interface defects can respond dynamically at the ac frequency. A detailed comparison between the standard C-V and DLCP profiles can thus often distinguish interface states from bulk defects in the semiconductor film.

1.3 Transient Photocapacitance Spectroscopy

Transient photocapacitance has become a well-established characterization technique in the field of amorphous semiconductors where it has been used to establish the continuous spectrum of defect levels in the bulk [6] as well as anomalous interface defects [7]. While the drive-level method yields values for the absolute number of midgap states in a material as well as offering the capability of spatial profiling the defect densities throughout a sample, photocapacitance yields high-resolution descriptions of the shape of the electronic density of states. Thus photocapacitance is a powerful tool for examining qualitative trends in the energy distribution of defect states with changes in, for example, deposition parameters.

The principle and implementation of the photocapacitance method is similar to the more familiar DLTS technique. The semiconductor junction held under reverse bias is subjected periodically to a voltage "filling pulse" which allows majority carriers to move into the previously depleted region and be captured. Following these pulses a capacitance transient can be observed as holes are thermally emitted out of the majority carrier traps and leave the depletion region. In the TPC measurement, however, one introduces sub-band-gap monochromatic light to induce optical transitions in addition to any thermal ones. Actually, light is applied after *every other* filling pulse so that the capacitance transients with and without light present can be subtracted. The difference, integrated over a time window and normalized to the photon flux, yields the photocapacitance signal at each photon energy selected by the monochromator. Repeating this over the full range of sub-band-gap photon energies available yields the *photocapacitance spectrum*.

The same sample structure is used in a photocapacitance as for the drive level capacitance profiling measurement. However, because a proper combination of voltage levels and light intensity must be used to produce analyzable data, photocapacitance is a much more difficult technique to implement than drive level profiling. The method is extremely valuable, however, since these high-resolution spectra can determine the qualitative shape of the electronic density of state, identify prominent features associated with defect levels, and track the growth, suppression or energetic changes in these levels as a function of alloy composition.

1.4 CIGS Sample Synthesis

Elementally modulated reactants were used to prepare thin films of $CuIn_{1-x}Ga_xSe_2$. The elementally modulated reactants were prepared using thin film deposition techniques [8] and consist of Ångstrom scale layers of the elements to be reacted. The multilayer repeat distance, which can be continuously varied, determines the diffusion distances and subsequent reaction parameters of temperature and time required for complete reaction. The total film thickness is the product of the number of multilayer repeats and the thickness of the multilayer repeating unit. The elementally modulated samples are removed from the vacuum chamber to be processed. This growth technique is easily scalable.

3

Several in-situ probes are available as a result of the layered structure of the elementally modulated reactants. The short diffusion distances in the multilayer reactants result in low reaction temperatures and rapid reaction rates allowing the energetic changes occurring in the reactions to be followed using scanning calorimetry [9, 10]. The modulated nature of the reactant produces a low angle x-ray diffraction pattern which, collected as a function of temperature and time, permits the interdiffusion of the reactant to be characterized quantitatively[11, 12, 13]. High angle diffraction combined with scanning and transmission electron microscopy are used to determine the structure and morphology of crystalline products and the absence of crystalline compounds in amorphous intermediates. These techniques provide detailed information about the reaction pathway.

2.0 SAMPLES FROM EXTERNAL SOURCES

In addition to the CIGS material synthesized at the University of Oregon, a number of $CuIn_{1-x}Ga_xSe_2$ (CIGS) and $CuIn_{1-x}Al_xSe_2$ (CIAS) samples were obtained from Bill Shafarman at the University of Delaware (Institute of Energy Conversion). These samples were characterized by the experimental techniques described above to establish a baseline to compare with material being developed at Oregon. These films were grown about 2 μm thick using four-source elemental evaporation [14,15]. The film compositions, determined by energy dispersive x-ray spectroscopy, are slightly Cu poor, with Cu/(In+Ga)=0.8-0.9.

The IEC samples were in the form of finished solar cells. The films were deposited on soda-lime glass which had been coated with a 1 μm Mo layer. To form devices, a chemical bath deposition was used to deposit 30-40 nm of CdS, then ZnO:Al was sputtered to form the top contact, with evaporated Ni/Al grids.

The CIGS films obtained from IEC were prepared with Ga fractions ranging between 0 and 0.8 and are listed in Table I. A majority of the CIGS samples studied had ratios of Ga/(In+Ga)=0.3, resulting in a bandgap, E_g, near 1.2 eV. Although most of the CIGS films were deposited at 550^oC, one sample was prepared with T_{ss} = 480 °C and one with T_{ss} = 400 °C. Auger depth profiles indicated uniform Ga compositions in all cases.

The four CIAS films studied were also deposited using 4-source elemental evaporation, but at a slightly lower substrate temperature of 450 ºC. The CIAS films were typically grown to about 2-3 μm of thickness. X-ray diffraction studies have verified that these CIAS films are single phase. Their elemental composition was again determined using energy dispersive x-ray spectroscopy and this revealed that their Al fractions ranged between 0.13 to 0.48. The corresponding bandgaps, estimated from quantum efficiency measurements, ranged from 1.15 eV to 1.67 eV. The device performance parameters for the CIAS devices are listed in Table II.

In addition to the polycrystalline CIGS and CIAS obtained from University of Delaware, we also obtained a couple of epitaxial single crystal films from the group of Angus Rockett at the University of Illinois. These were deposited onto a (110) oriented GaAs substrate. The CdS and ZnO top contacts were added at IEC using the same methods as for the polycrystalline samples. The single crystal sample examined for this report had a gallium content of 0.3.

4

Table I. CIGS devices studied from IEC, in order from lowest to highest Ga content, together with their properties. These include the substrate temperature during growth of the CIGS layer (T_{SS}), the Ga content, and the optical gap (E_g). Also listed are the device performance characteristics: the efficiency, open circuit voltage (V_{oc}), short circuit current (J_{sc}) and the fill factor (*FF*).

Sample #	T_{ss} (ºC)	E_g (eV)	Ga/(In+Ga)	*Eff* (%)	V_{oc} (V)	J_{sc} (mA/cm^2)	FF (%)
D469	550	1.0	0.0	11.3	0.46	36.8	66.6
D008	550	1.0	0.0	9.5	0.41	34.8	65.6
D982	550	1.16	0.27	11.0	0.53	33.3	62.6
D362	550	1.16	0.27	11.2	0.53	32.9	63.8
D456	550	1.16	0.27	11.6	0.55	32.4	65.0
D427	550	1.18	0.29	14.5	0.61	31.7	74.7
D934	550	1.18	0.30	14.9	0.63	30.6	76.8
D934	550	1.18	0.30	15.2	0.63	31.5	76.7
D400	550	1.20	0.32	16.1	0.65	33.0	74.8
D233	480	1.19	0.32	14.3	0.61	32.3	72.2
D264	400	1.20	0.32	11.8	0.60	29.5	65.7
D988	550	1.29	0.46	15.2	0.72	29.1	72.5
D915	550	1.42	0.65	12.2	0.78	23.6	65.5
D912	550	1.53	0.80	8.8	0.82	16.3	65.9

Table II. CIAS devices studied from IEC, in order from lowest to highest Al content, together with their properties. The device performance characteristics: are also given.

Al/(In+Al)	E_G (eV)	V_{OC} (V)	J_{SC} (mA/cm^2)	FF (%)	*Eff.* (%)
0.13	1.15	0.59	34.2	65	13.1
0.29	1.36	0.71	25.3	63	11.3
0.35	1.45	0.72	21	64	9.6
0.48	1.67	0.72	16.9	63	6.3

3.0 RESULTS

3.1 Photocapacitance Studies of Polycrystalline and Epitaxial (CIGS) Alloy Films

First we compare and contrast results obtained from characterization studies of polycrystalline CIGS samples obtained from Bill Shafarman's laboratory at the University of Delaware, and of epitaxial single crystal films from Angus Rockett's growth system at the University of Illinois using the photocapacitance method. The photocapacitance spectra were recorded at 150 K under similar conditions. Samples were held at 1 V reverse bias, and subjected to 50 msec filling pulses to 0 V bias. The transient response to this voltage pulse was

FIG 1. The transient photocapacitance spectra for the University of Illinois single crystal device (closed symbols) and the IEC polycrystalline device (open symbols) appear very similar, and indicate nearly the same deep defect bands.
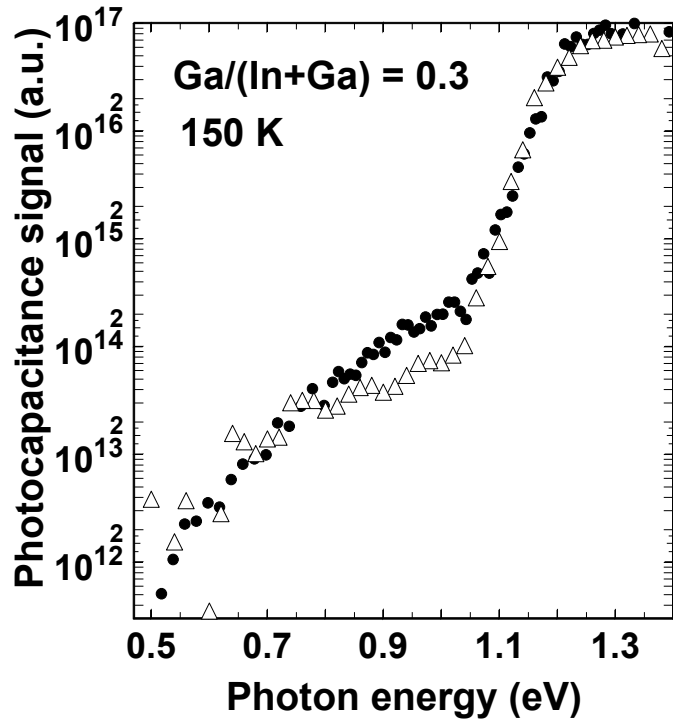
integrated over a boxcar of width 250 msec, centered 275 msec from the start of the transient. Since the capacitance transient response is enhanced by the presence of light (the TPC signal is positive), the observed transitions result from the optical excitation of trapped holes from the defects into the valence band. Spectra have also been collected using a range of reverse biases and filling pulses. By studying the effect of these parameters on TPC signal magnitude, we have verified that the sub-bandgap response that we observe is due to the CIGS absorber layer and does *not* originate from the thin, fully depleted CdS layer.

The appearance of our TPC spectra greatly resembles sub-band-gap optical absorption spectra. A comparison between TPC spectra of the single crystal device and the IEC polycrystalline device of comparable Ga content is shown in Figure 1. These spectra are remarkably similar despite the differences in substrate and growth technique. Clearly, then, the deep defect response that is exhibited (the choulder extending from 1.0eV to lower energies) does not originate solely from grain boundaries, but is characteristic of the bulk material. However, the single crystal sample does show a larger defect response in the energy regime near 0.9 eV, which is not observed in polycrystalline material. The width of the bandtail slope, as characterized by Urbach energy E_U, generally indicates the degree of alloy disorder in chalcopyrite semiconductors [16] and corresponds to the broader of the conduction or valence band edges. In such CIGS devices, the data in Fig. 1 clearly also indicate that E_U is not strongly affected by the grain boundaries.

By obtaining TPC spectra over a range of temperatures we have verified that the 0.8 eV defect is unlikely to correspond to the predominant hole trap observed using admittance techniques, which has a thermal activation energy between 0.1 and 0.3 eV. Such trap states are indeed observed in the admittance spectra of all of our samples. However, the relative

6

FIG 2. Transient photocapacitance spectra for the IEC polycrystalline samples with Ga contents ranging from Ga/(In+Ga) = 0 to 0.8. These have been aligned to emphasize the similarity of the deep defect response. Fits (solid lines) are obtained using a single Gaussian defect band, centered at 0.8 eV, plus an exponential band of tail states. These are shown in dashed lines for the Ga/(In+Ga) = 0.3 sample.
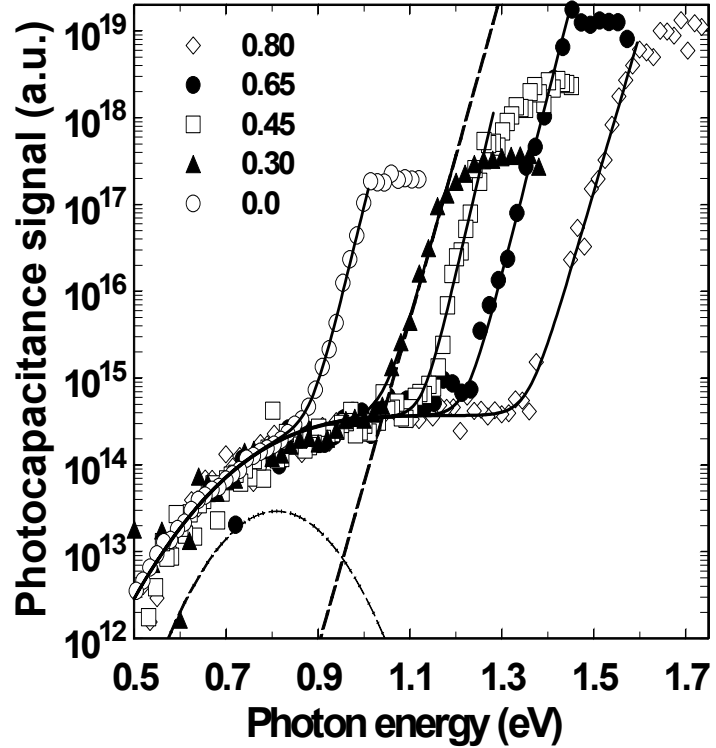
magnitudes of the defects deduced by the two methods are not correlated. TPC spectra for a range of the IEC polycrystalline devices with different Ga fractions are shown in Fig. 2. These films have Ga fractions varying between 0% to 80at.%. The spectra have been aligned to emphasize the similarity of the deep defect band which, in all cases, has been fit using the same Gaussian deep defect band, centered at 0.8±0.05 eV with width 0.13 eV.

The fact that the deep defect transition appears to be independent of Ga fraction is consistent with the behavior predicted for many classes of defects in CIGS, including metal vacancies and metal antisite defects.[17] However, the observed 0.8 eV transition energy does not currently match any of the theoretical predictions for those types of defects. The estimated magnitudes of the 0.8eV defect band, determined from these TPC spectra together with auxiliary measurements, are listed in Table III along with the Urbach energies characterizing the exponential bandtail portion of these spectra.

TABLE III. Relative deep defect densities and Urbach energies estimated from the TPC measurements of the CIGS samples. All of these were IEC polycrystalline films except for the final entry which was an epitaxial film deposited at the University of Illinois.

Ga/(In+Ga)	N_D (a.u.)	E_U (meV)
0.0	2	18
0.3	8	23
0.45	0.3	19
0.65	0.4	21
0.8	0.7	24
0.3 (crys)	--	26

FIG 3. Schematic of observed defect bands in low and high Ga alloys. Optical transitions are shown with wavy lines and thermal transitions with straight lines. The thermal transition, shown here at 0.2 eV, actually varies from 0.1 to 0.3 eV depending on the sample.
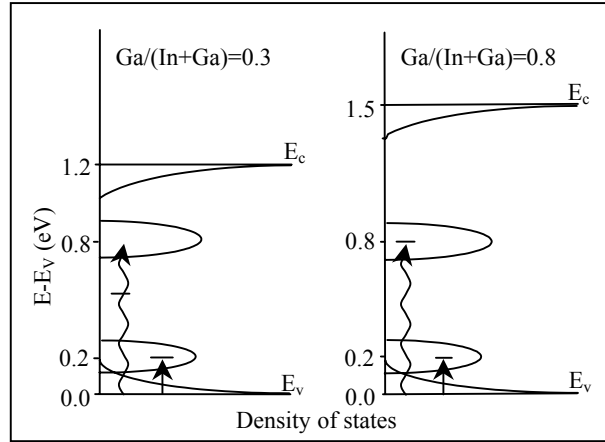
Although the defect density associated with the 0.8 eV transition does not change systematically with Ga content, it approaches mid-gap in the high Ga material as illustrated in Figure 3. This means it would become a much more efficient recombination center in the high Ga alloys.

3.2 Studies of CIGS Alloy Films Under Varying Growth Conditions

To explore the effect of growth conditions on defect densities and resulting cell efficiencies, we investigated a set of samples from IEC that all had similar Ga fractions; however, they were deposited at varying growth conditions so that both the grain sizes and the devices performance varied substantially. We wanted to determine whether our characterization of the electronic properties of these films might indicate anything specific that could be linked to the variation in the device performance.

The transient photocapacitance (TPC) and transient photocurrent (TPI) spectroscopic techniques have been discussed in detail in our previous quarterly reports. The TPC and TPI spectra resemble optical absorption spectra, but with a sensitivity to signals ranging over more than five orders of magnitude, allowing the weak response from defects deep within the gap to be detected. These spectra also give a very accurate measurement of the slope of the band tail (the Urbach energy).

One important difference between the TPC (or TPI) spectra and optical absorption spectra is the dependence of the TPC and TPI spectra on the carrier mobilities. Changes in capacitance are due to net charge change within the sample, so that the TPC signal is proportional to *p minus n* where p is the number of holes collected and n the number of electrons. However, the TPI signal, due to total charges collected, is proportional to *p plus n*. Therefore, as discussed previously, this difference between TPC and TPI spectra allows the calculation of the minority carrier mobility-lifetime product, $(\mu\tau)_e$. An example comparison of these two types of spectra for one CIGS sample is shown in Fig. 5.

Such comparisons between the TPC and TPI spectra indicate that the minority carrier collection in typical devices is very good, with $n/p > 0.95$, corresponding to $(\mu\tau)_e \approx 2 \times 10^{-9}$ cm^2/V. This is despite our low measurement temperatures (150K) and limited collection times of 275 ms. However, the minority carrier collection in the lowest T_{ss} sample seems to be significantly

Table IV. Summary of device performance and minority carrier collection for a series of devices grown under varying substrate temperatures, T_{SS}. All devices were found to have negligable shunt loss and comparable series resistances.

T_{SS} (K)	Eff	J_{sc} (mA/cm^2)	V_{oc} (V)	FF	*n/p*
550	16.1	33.0	0.65	74.8	0.99
550	14.7	30.0	0.63	77.3	0.99
550	14.5	31.7	0.61	74.7	0.98
550	11.6	32.4	0.55	65.0	0.97
550	11.2	32.9	0.53	63.8	0.97
480	14.3	32.3	0.61	72.2	0.92
400	11.8	29.5	0.60	65.7	<0.90

worse, with *n/p* less than 0.9. A summary of the device performance and *n/p* results is given in Table IV. In Figure 5 we plot the device efficiencies vs. the deduce n/p collection efficiencies for the 0.3 Ga fraction devices deposited at 550oC. A fairly strong correlation is indicated. However, it is interesting to note (see Table IV) that there are also cases where the efficiencies of these devices can be high in spite of a relatively low deduced value of n/p.
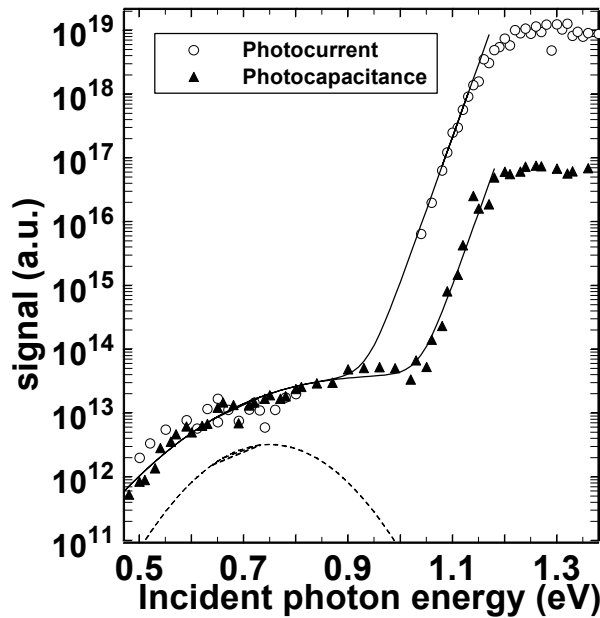
FIG. 4. Photocapacitance spectrum (closed symbols) and photocurrent spectrum (open symbols) for $CuIn_{0.7}Ga_{0.3}Se_2$ device D934, showing the difference between these spectra caused by minority carrier collection. Fits (solid lines), again result from the sum of a gaussian band of defect states and an exponential band of tail states.
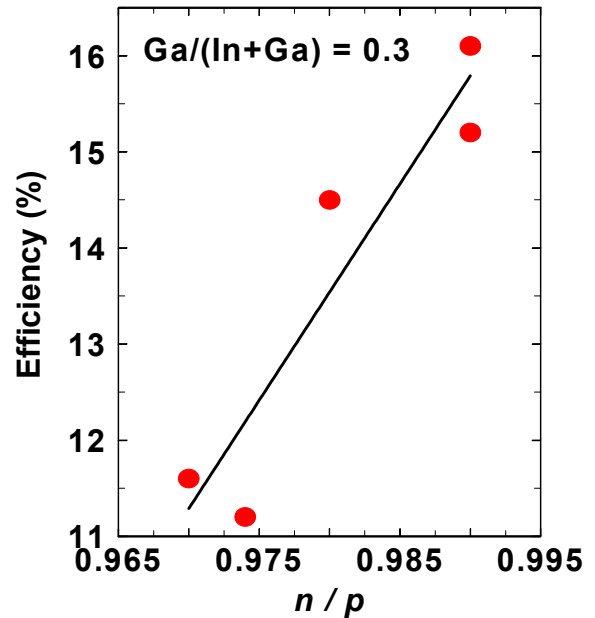
FIG. 5. Cell efficiencies vs. minority carrier collection ratios, n/p, for five 30% Ga fraction devices deposited at 550°C. For these samples a fairly good correlation appears to be exhibited.

FIG. 6. Photocapacitance spectra for CIGS devices grown under different conditions. Note that the spectrum shown in solid triangles is from a device with Ga/(In+Ga)=0.8. Otherwise, devices shown have Ga/(In+Ga)=0.3.
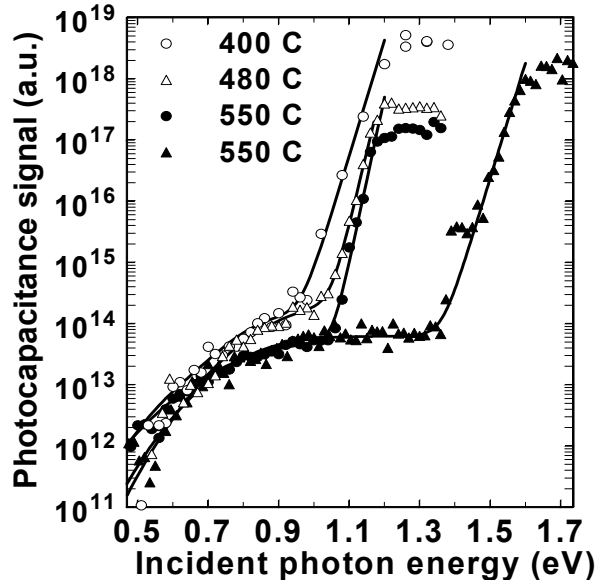
In Fig. 6, TPC results for samples deposited at several different temperatures are compared. These spectra have been aligned such that the magnitude of their associated photocurrent spectra is the same (10^{19} units on the vertical scale of Fig. 6) at 1.2 eV. Then, the samples exhibiting *lower* TPC signals at 1.2 eV correspond to those with *better* minority carrier collection. The relatively high value of the TPC signal at 1.2 eV for low T_{ss} samples, as well as for the high Ga sample, indicates a low minority carrier collection efficiency compared to the other devices.

We now briefly discuss the deep defect band portion of these TPC spectra. We have found that the TPC spectra for all the CIGS devices we have measured to date clearly fall into two distinct classes. Those for low T_{SS} (also those for epitaxial single crystal films as discussed in our last Quarterly Report for 2000) have a distinctly stronger response in the 0.8-0.9 eV energy range than spectra of the other devices. This is clearly exhibited in Fig. 6. We fit such TPC spectra assuming an exponential distribution of band tail states and one or more Gaussian bands of defect states. Spectra for devices with a wide range of Ga contents were previously successfully fit using a single broad Gaussian defect band centered around 0.8 ± 0.05 eV from the valence band and with FWHM 0.26 eV. In all devices grown with high T_{SS} and Ga/(In+Ga)=0.3, the magnitude of this defect band seems to vary by less than a factor of two.

The data from the low T_{SS} material could indicate a shift in this broad defect band towards deeper energies, around 0.9 eV. However, the spectra have been fit more successfully using two narrow, overlapping Gaussian defect bands whose relative magnitude is altered depending on the growth conditions. The current set of data does not tightly constrain the many possible parameters of such a fit; however, we have had the most success using Gaussian bands centered at 0.67 eV and 0.85 ± 0.05 eV, with widths of 0.09 eV. In this scenario, the relative size of the two bands would be nearly identical in typical material, but in the low T_{SS} polycrystalline material and in epitaxial single crystal material, the deeper 0.85 eV band is 5 to 10 times larger than the 0.67 eV band.

One other intriguing correlation has been identified from information obtain by the photocapacitance spectra on CIGS material and device performance. In Fig. 7 we plot the photovoltaic device short-circuit current density versus the Urbach energies (the characteristic

FIG. 7. Correlation of device short circuit current and Urbach energy determined from TPC spectra for 30at.% Ga CIGS samples. The triangular symbols indicate samples deposited at 550°C at IEC while the boxes indicate samples deposited at temperatures below 500°C. The diamond is a device fabricated out of an epitaxial single crystal CIGS film deposited at the University of Illinois.
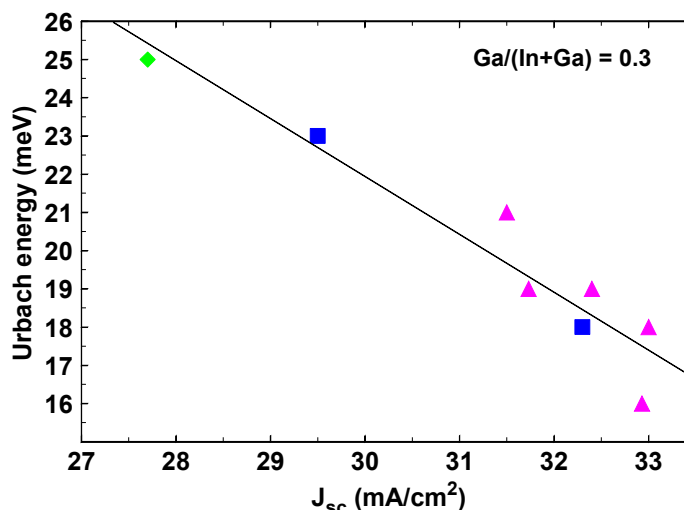
slope of the exponential bandtails obtained from the data for the 30at.% Ga alloy samples in Figs. 1,2, and 6). Quite surprisingly we find a very strong correlation. This is not understood at present, but might be related to the fact that the bandtail widths disclose the distribution of states extending from the conduction band into the gap, and that these states control the minority carrier mobilities and hence the short circuit current.

We also carried out admittance spectroscopy on these devices. Data for the 480°C deposited devices are displayed in Figure 8. Other groups have reported two types of deep defects that act as majority carrier traps from such measurements of CIGS films. The magnitude of a defect band at 0.3 eV has been linked to device efficiencies by the University of Stuttgart group.[18] However, we do not typically observe such a defect response in the IEC devices. A shallower defect *is* observed in our devices with E_a varying between 0.1 and 0.3 eV. Such a defect has been reported previously and so, to be consistent with this previous work, we will label this defect as

FIG. 8. Admittance spectroscopy results for a device fabricated with a substrate temperature of 480 °C, showing a large capacitance step from 20 nF/cm^2 to 37 nF/cm^2 corresponding to an activation energy of E_a=0.17 eV, plus a deeper, broader step from 37 nF/cm^2 to 58 nF/cm^2 corresponding to a response near mid-gap.

11
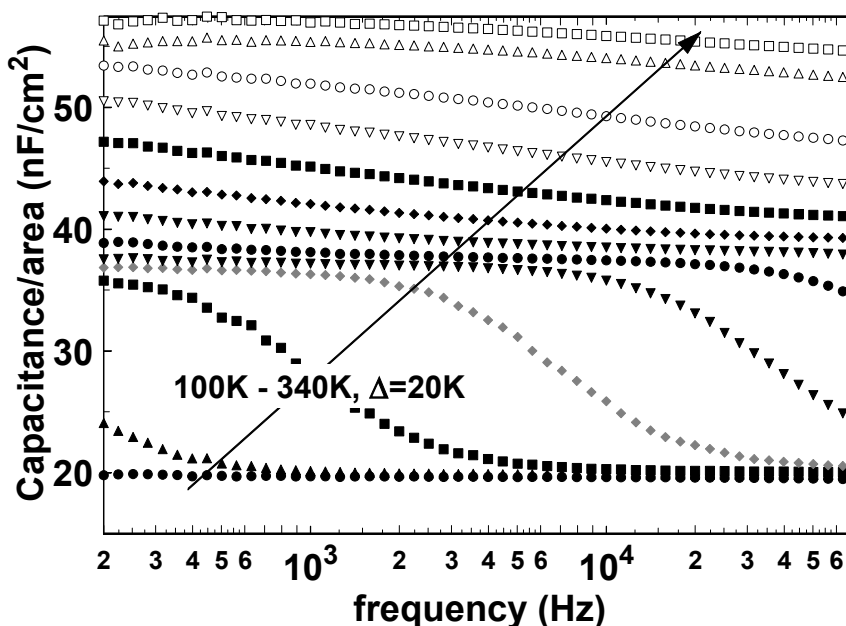
"N1". Its response energy has been found to vary between devices, and even within the same device after subjecting it to various heat treatments or light soaking. However, because the activation energy and prefactor for this defect follow the Meyer-Neldel rule, it is thought to be physically the same defect. We have found that all of our results in the IEC high T_{SS} material reveal such an N1 defect consistent with the results of these other groups.

Although this defect was attributed to an electron trap at the interface by Herberholtz and co-workers in Germany [19], the magnitude of the capacitance step in our samples argues against this interpretation. For example, in the device shown in Fig. 8, the capacitance/area changes from 20 nF/cm^2 to 37 nF/cm^2, indicating the average capacitance response position $<x>$ changes from 0.51 μm to 0.28 μm. Since the 0.23 μm change in $<x>$ is 6-8 times the thickness of the CdS layer, it cannot be due solely to electron trapping originating from the n-type side of the junction.

In the samples grown with low T_{SS}, we have observed an additional defect response near mid gap, around 0.54 eV. This could have two possible origins. It could indicate an additional defect frozen in by the lower growth temperatures, possibly associated with the larger fraction of sample volume near grain boundaries. Alternatively, it could reflect a minority trapping process at the interface. This latter possibility is related to the fact that the thermal generation of electron and hole pairs occurs at a characteristic thermal energy of $E_g/2$ in the depletion region. Therefore these thermally generated electrons could end up in minority carrier traps near the junction, giving a significant capacitance response with an activation energy near $E_g/2$.

In summary, two distinct sub-band-gap defect transitions are observed in $CuIn_{1-x}Ga_xSe_2$ devices deposited below 500°C. From our transient photocapacitance measurements it appears that one is centered roughly 0.8 eV from the valence band edge, while the other, observed using admittance spectroscopy, lies much closer to the valence band edge with an activation energy that varies between 0.1 and 0.3 eV. Moreover, for devices grown at relatively low substrate temperatures additional defect bands seem to appear, including an enhanced response deep within the gap, between 0.8 and 0.9 eV, and perhaps an additional defect band near mid-gap. At this time we have not been able to demonstrate that any one of these defects has a dominant effect on the device efficiencies. Nonetheless, we believe that all of them undoubtedly provide important pieces to the puzzle.

3.3 Drive-level Capacitance Profiling (DLCP) Studies of CIGS Alloy Films

A series of DLCP profiles taken at a series of different frequencies at fixed temperature (110K) is displayed in Fig. 9(a) for a $CuIn_{1-x}Ga_xSe$ device with $x = 0.3$. We see that, while there is a significant spatial dependence to the electronic properties for this sample, they are sufficiently slowly varying so that, with reasonable confidence, we may extract the integrated density of states *vs.* emission energy, $E_e = k_BT \ log(\nu/\omega)$, in the vicinity of a particular spatial location, say where $<x>$ is near 0.4 μm. These extracted data are displayed as solid circles in Fig. 9(b). Comparing these data with Eq. 4 suggests that the free carrier density (obtained in the low E_e limit) is roughly 3.5 x 10^{15} cm^{-3}, and that there is a deeper defect with a thermal emission energy near 0.1 eV of density 3.3 x 10^{15} cm^{-3}. This is seen more clearly by the dotted curve in Fig. 9(b) which represents the derivative of the solid line with respect to E_e; that is, the density of states. Finally, the triangles plotted on top of the dotted curve indicate the dependence of

$-\omega\, dC/d\omega$ obtained from admittance spectroscopy data of this sample under zero volts dc bias. These data have been rescaled to match the magnitude of the dotted curve. Thus we see quite good agreement between the DLCP determination of the density of states and the data obtained from admittance spectroscopy measurements. However, considerably more information about the electronic properties of the sample has been deduced from DLCP; specifically, we can assess the spatial uniformity of the deduced defect distribution, and we obtain a direct quantitative value for the defect's density. Indeed, in samples where there the spatial variation of properties is more pronounced, the use of admittance spectroscopy to deduce the density of states can actually lead to very large errors.
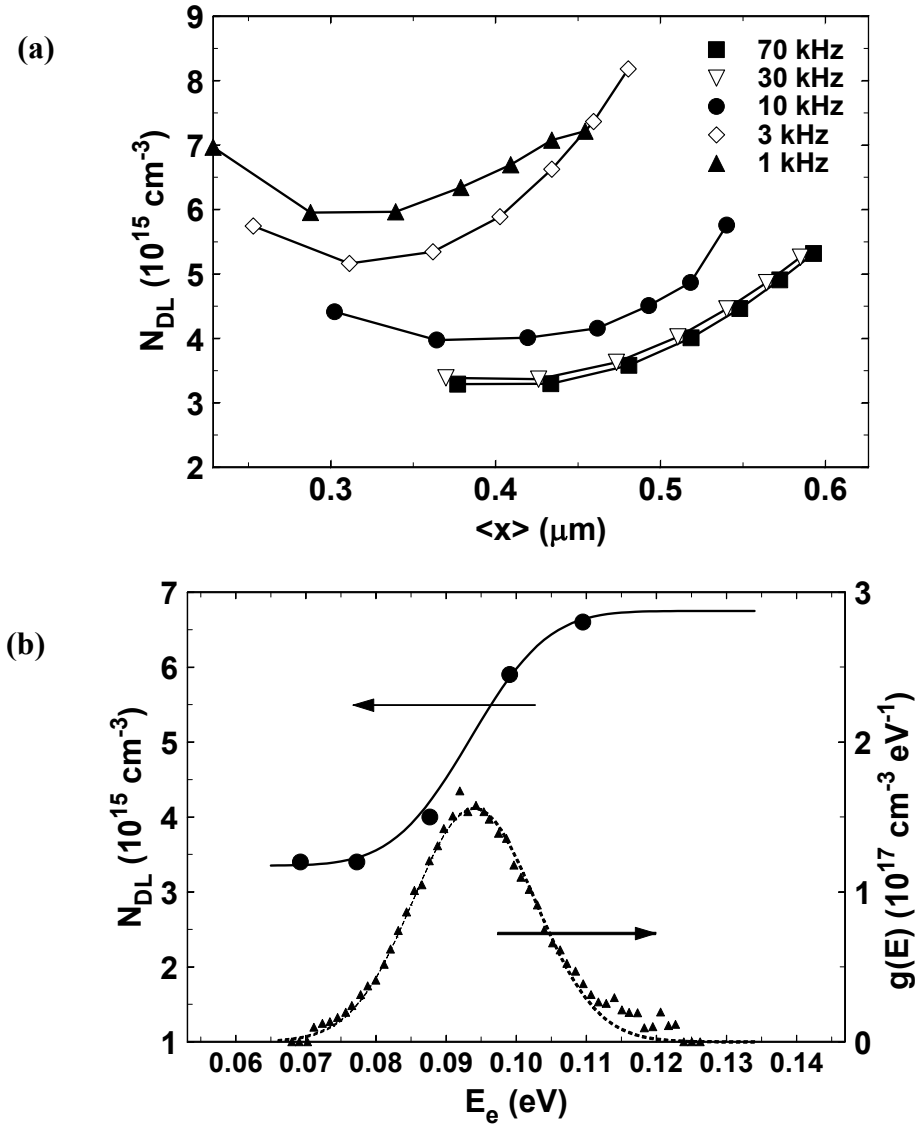
FIG. 9. **(a)** Typical DLCP profiles, taken at 110 K for several frequencies as noted in the figure. This device was prepared using T_{ss} = 550 °C. **(b)** Plot of the DLCP value at $\langle x \rangle$ = 0.4μm versus thermal energy E_e, showing more clearly the thermal activation of the defect. E_e was calculated using Eq.1, with $\nu = 5.4 \times 10^4\, T^2\, \mathrm{s}^{-1}$ obtained from admittance spectroscopy. The fit to the DLCP response, shown by the solid line, assumes a gaussian shape which corresponds in position and width to the AS data ($\omega\, dC/d\omega$, triangles, scaled in magnitude to match the DLCP result).

13

The quantitative accuracy of the DLCP measurement was previously demonstrated for the D_0 center in amorphous silicon films by comparing results using electron spin resonance (ESR) measurements with DLCP in a-Si:H/Pd Schottky devices [20]. Since DLCP can only examine deep states between E_F and E_e, and because the D_0 center lies very near mid-gap in a-Si:H, it was recognized that the DLCP measurement was probably not capable of recording the entire defect response from that center. For this reason, in Ref.20, the total defect density was estimated to be *twice* the measured DLCP defect density determined at the position of maximum slope in the N_{DL} versus E_e data. Following this procedure, excellent agreement was obtained between ESR and DLCP estimates for the D_0 density in a-Si:H; to within a factor of 1.3. Unlike the case of a-Si:H films, the predominant deep defect response in CIGS films is much shallower than mid-gap, and we believe that DLCP is able to detect the entire band. Thus, the defect densities deduced from DLCP for our CIGS samples will the *difference* between the saturated maximum N_{DL} values, at high E_e, and the estimated free carrier density, obtained from the low E_e limit of N_{DL}.

FIG. 10. Comparing *C-V* and DLCP results for a CIS device. These data were taken at 11 kHz for the series of temperatures noted in the figure. **(a)** *C-V* results for device D008. **(b)** Results of DLCP measurements on the same device.

As a second example we display, in Fig. 10, a direct comparison between the standard C-V profiles with the DLCP profiles for a sample containing 0% Ga (that is, for a CuInSe$_2$ device). In this case we have varied E_e by examining profiles at fixed frequency (11kHz) but over a range of measurement temperatures. We estimate that for 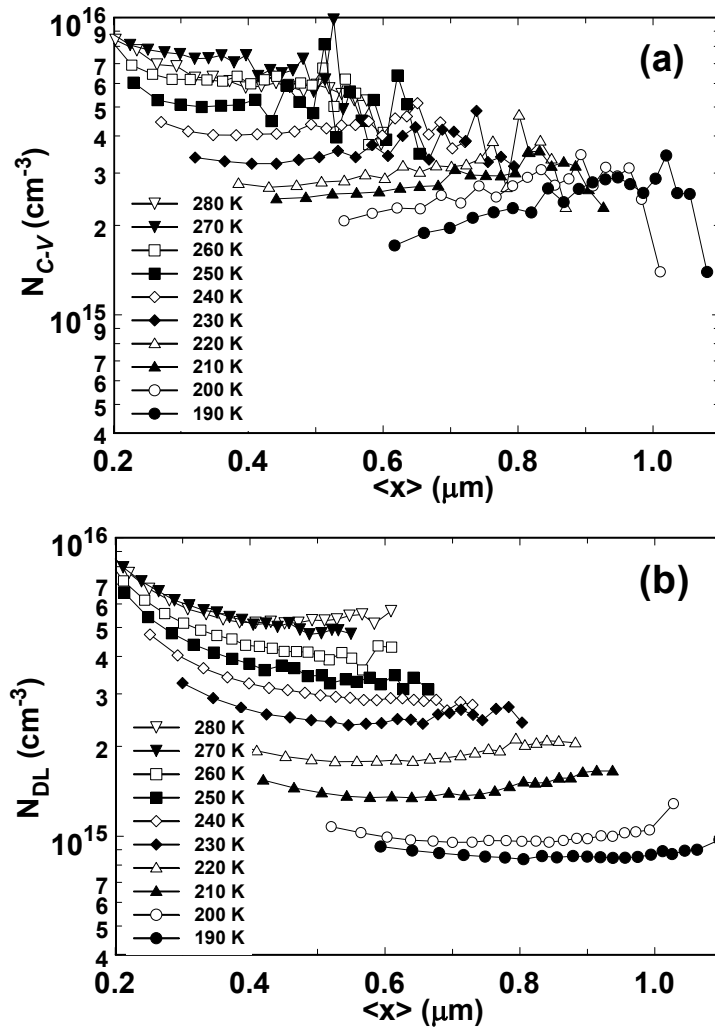this sample the lowest temperature profile at 190K corresponds to a value of E_e of 0.25eV, while the highest temperature (280K) corresponds to about 0.36eV. Admittance spectroscopy for this device indicates a deep defect with a characteristic energy near 0.3eV; thus, our range of profiles spans the energy response of this center. Indeed, we see that both the high and low temperatures DLCP profiles in Fig. 10(b) each appear to reach a limiting value. The low temperature value of slightly below 10^{15} cm^{-3} thus indicates our best estimate for the free carrier density, while the *difference* between the high and low temperature DLCP profiles (of roughly 5 x 10^{15} cm^{-3}) gives us the density of the deep defect itself.

Such estimates would be much more difficult based upon the C-V profiles of Fig. 10(a). Even at the lowest temperatures we would overestimate the free carrier density by more than a factor of 2 and also judge it to be quite non-uniform. Both of these conclusions would be false based upon the DLCP profiles. Also, the uniformity of the deep defect response indicated for the highest temperature profiles differ substantially for the C-V *vs*. DLCP results: DLCP indicates a definite increase as we move within 0.4 μm of the barrier junction, while the C-V results appear much more uniform. It is actually quite interesting to compare these two sets of profiles with the simulated profiles given in Fig. 13 in Section 3.4 below since many aspects of that simulation are mirrored in these actual data. Note, however, the C-V profiles do not indicate a specific feature at low applied bias resembling the portion of the simulated response [Fig.13(a)] that was due to an assumed interface state.

Finally we should mention that, for all devices studied, the admittance spectra have indicated an activation energy of conduction well below 100 meV. This means that conduction cannot be frozen out using the range of temperatures and frequencies currently available to us, and so we can only set an upper limit on the value of the actual free carrier density.

3.4 Numerical Modeling of Admittance and Capacitance Profiling Measurements

To provide additional insight into the results of the previous Section, we have obtained numerical solutions of Poisson's equation for various types of n^+-p junctions to directly demonstrate the advantages of the DLCP method over standard *C-V* profiling. Results presented here are for a model semiconducting junction in which the p-type film contains two spatially uniform features: a gaussian band of deep acceptor-like defects and a shallow acceptor band giving rise to a specific density of free carriers. In this model, the p-type film also contains a spatially non-uniform band of deep states near the barrier interface. For this model, illustrated in Fig. 11, specific parameters have been chosen to lie in a range corresponding with experimental data on actual thin film CIGS photovoltaic junctions. It is worth mentioning that we may also easily incorporate spatial variations of the deep defect density, the shallow dopants, or both into these simulations.

Poisson's equation becomes an integral-differential equation under such conditions. The numerical solution utilizes a modified Noumerov method which has been described in detail previously [4]. For the present study, we solve the Poisson equation first at the nominal dc bias, and then add several values of δV. Each value of δV results in a change of total charge, δQ,

which is found by numerically integrating over the entire depletion region. The temperature and frequency response is incorporated by imposing an emission time limit for the gap state response. Capacitance (C_0) is then determined by computing $\delta Q/\delta V$ for a very small value of δV (typically a few mV), and C_1 is found by repeating the calculation for larger values of δV. Thus, the numerical calculation simply relies on Poisson's equation and the validity of $\delta Q/\delta V$ with an emission time limit to deduce the junction capacitance.

The result of a simulated admittance spectrum based upon the model junction of Fig. 11 is displayed in Fig. 12. One clearly observes a two peak structure in the frequency derivative of capacitance: The higher frequency peak is due to the deep bulk defect level, while the lower frequency peak comes from the states at the barrier interface. Clearly, either feature could not be
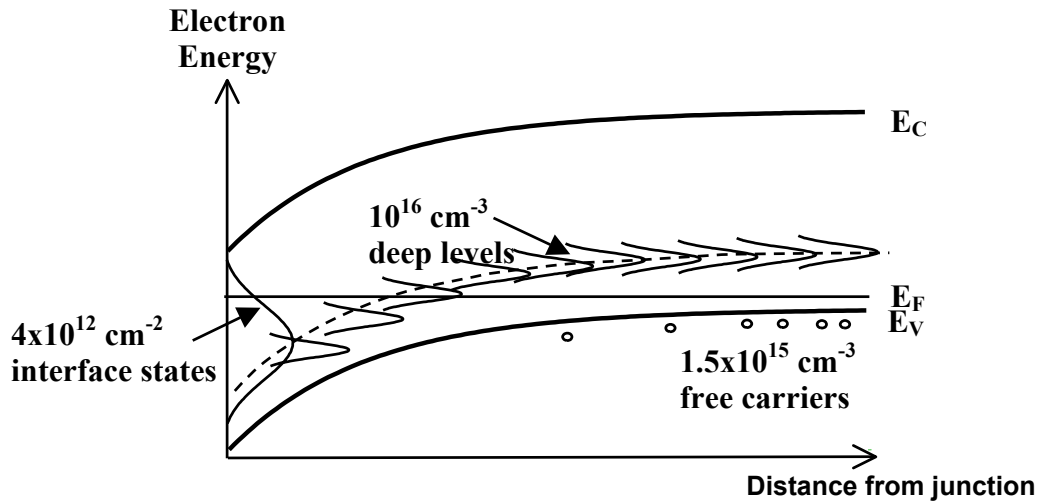
FIG. 11. Schematic of model semiconductor junction consisting of a lightly p-type semi-conductor with a free hole density of 1.5×10^{15} cm^{-3}, a deep acceptor defect at $E_V + 0.3$eV with a density of 1×10^{16} cm^{-3}, plus a band of interface states of density 4×10^{12} cm^{-2} with roughly the energy distribution indicated. The n$^+$ side of the junction is not shown.
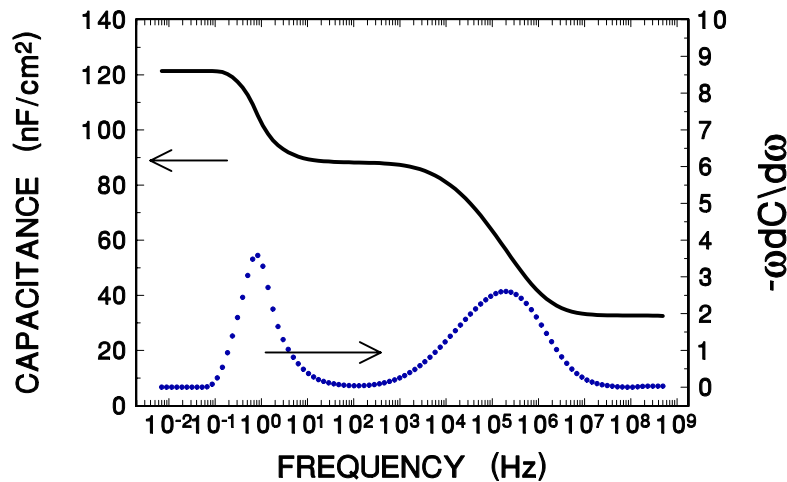
FIG. 12. Simulated admittance spectrum under 0V bias for the model semiconductor junction of Fig. 11 with a built-in potential of 0.55 volts. We assumed a temperature of 290K and an emission prefactor of $(7.5 \times 10^6$ s^{-1} K$^{-2})T^2$ for both interfacial and bulk defects.

identified as a bulk or interface feature from such a spectrum by itself; however, by repeating these measurements at various applied dc biases this issue can be resolved, at least in principle. It is thus unfortunate that almost all admittance spectra reported from studies of CIGS generally have only presented experimental results for zero applied bias conditions.

A set of simulated *C-V* profiles for this model semiconductor junction is displayed in Fig. 13(a). This simulation clearly demonstrates that both the deep states and the interface states have
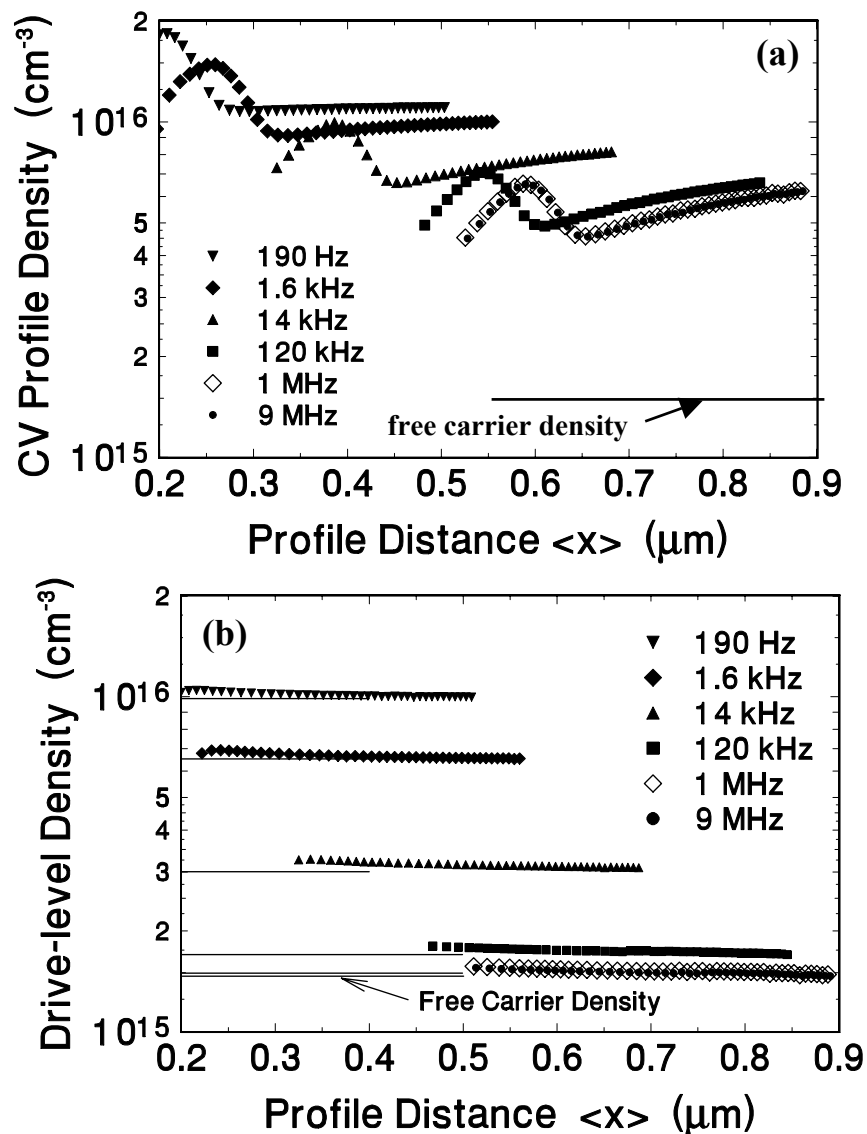
FIG. 13. (a) Simulated *C-V* profiles for different frequencies at 290K obtained from the model *n*+-*p* junction shown in Fig. 11. Note that none of these profiles provide a meaningful estimate of the density of free carriers shown by the thin solid line. Also note the influence of the interface states on the shapes of these profiles. **(b)** DCLP profiles calculated under the same conditions. The thin solid lines indicate the theoretical value these profiles should have as given by Eq. 4. Note that in this case the highest frequency profiles accurately reflect the density of free carriers, and that there is almost no influence from the interface states.

a profound influence on the *C-V* profiles. In particular, their influence almost completely precludes an accurate measurement of the free carrier density by this method.

In Fig. 13(b) we display the simulation of a DLCP measurement. As expected, the profile for the largest values of E_e (smallest frequency) most closely agree with the *C-V* results, and accurately reflect the maximum density of states that can respond to the alternating component of bias: deep states plus shallow acceptors. However, in the low E_e limit (highest frequencies), the DLCP measurement discloses a much smaller density than *C-V*, and this accurately reflects the density of free carriers. This is because DLCP is a purely dynamic measurement so that, while the non-uniform, static charge density created by the ionized deep defects influence the value of the depletion width, *W*, it does not affect the value of N_{DL}. For the same reason, DLCP is insensitive to interface states, which clearly influences the *C-V* results shown in Fig. 13(a). This attribute of DLCP has previously been discussed in some detail (see Ref. 5).

3.5 CuIn$_{1-x}$Ga$_x$Se$_2$ (CIGS) Alloy Films – Metastability with respect to Light Exposure

An important aspect of CIGS devices to try to understand is the metastable behavior of these films with respect to prolonged light exposure with light matching the bandap. Because the DLCP method can be used to clearly identify whether changes in device properties occur within the bulk absorber vs. the barrier interface, we decided to examine this issue in a couple of the IEC CIGS sample devices.

Our light soaking treatment consists of exposure to optical excitation at 1064 nm and approximately 100 mW/cm^2, generated by a cw-YAG laser. Samples were typically exposed for 3 hours at 25 °C, then cooled immediately in the dark. We subsequently observed significant changes in the average depletion charge density and in the density of deep defects, as illustrated in Fig. 14. We can conclude that these changes definitely occur in the bulk region of the CIGS absorber. The observed metastable changes anneal away in the dark at elevated temperatures, with a time scale of several hours at 50 °C. We stress that our measurements gave absolutely no indication that interface states were introduced, or increased, by this light-soaking treatment.

Previous studies at other laboratories using red light exposure also noted an increase in depletion charge density, leading to a decreased depletion width and increased capacitance. [19,21] Those researchers attributed this to the metastable capture of photogenerated electrons by deep traps in the depletion region. The observed increased of free carrier density for our sample is not inconsistent with such a mechanism. Alternatively, our result could be due to a real increase in the density of shallow acceptors.

The observed increase in the deep traps for our sample, however, cannot be explained by such an electron capture mechanism. Moreover, our data indicate that in a given sample the free carrier density and the density of deep traps typically increase by a similar factors (usually about a factor of five), suggesting that the mechanisms behind these two types of changes may have a common origin.

The light-soaking treatment also caused a decrease in device efficiency (from 13% to 11%) largely due to a decrease in fill factor. This is illustrated in Fig. 15. Note that the beneficial effects of white light exposure on V_{oc} reported in other studies were not observed for the infared

FIG. 14. DLCP profiles, before and after light soaking, taken at 135 K. Note that the x-axes differ for the two sets of data. These profiles clearly illustrate a significant increase in carrier density (assumed to dominate the response at high frequencies) and also an increase in the deep trap density. This device was prepared using a substrate temperature of 400°C, but the metastable behavior observed is characteristic of all devices we've studied.
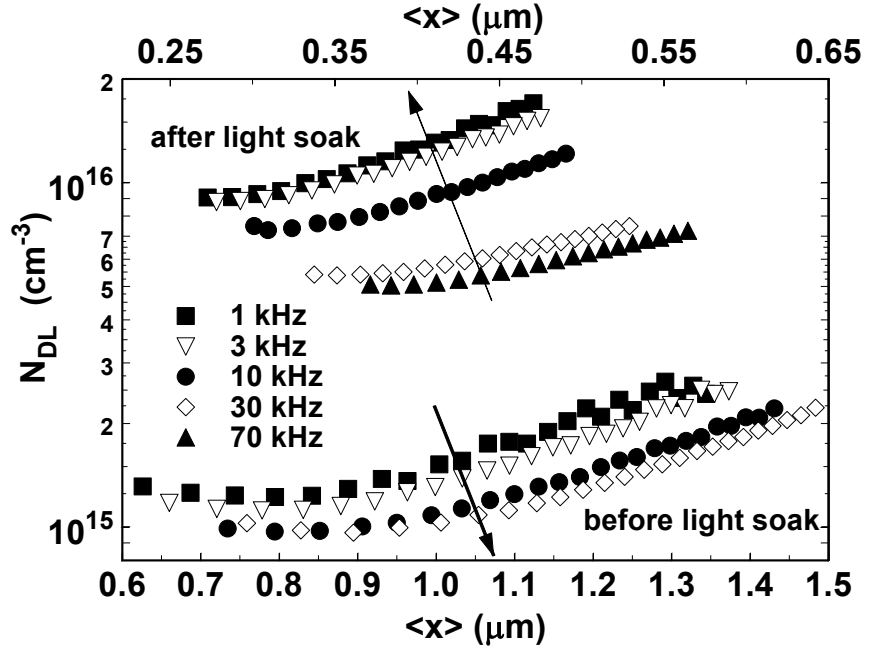
FIG. 15. Typical change in device performance before and after the long wavelength light soaking treatment. The overall efficiency was decreased from roughly 13% to 11%. A similar metastable change in performance was observed in all the devices studied.
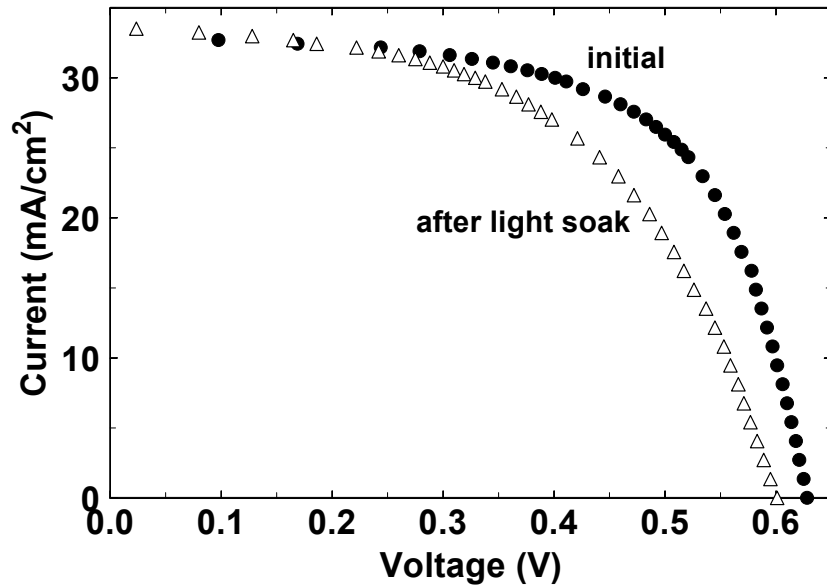
light soaking treatment we employed here, despite the large increase of carrier density. This is perhaps not surprising given the concurrent large increase in the deep defect density.

In conclusion, a band of deep defects has been identified in the bulk region of CIGS films which exhibits metastable changes upon optical exposure. We believe that these kinds of light soaking experiments may thus be quite valuable in identifying those defects which act as important recombination centers, if one can correlate changes in their density to changes in device performance. Using our ability to distinguish interface from bulk defects, and then relating different efficiencies and defect densities obtained within a single device, we thus hope to simplify the problem of identifying the most important defects that limit device performance.

3.6 Studies of CuIn$_{1-x}$Al$_x$Se$_2$ (CIAS) Alloy Films

We have carried out an experimental evaluation of the electronic properties of a series of four CuIn$_{1-x}$Al$_x$Se$_2$ (CIAS) alloy films provided to us by Bill Shafarman at IEC. This was accomplished by employing photocapacitance spectroscopy and drive-level capacitance profiling (DLCP). The CIAS photovoltaic devices for this study were prepared at IEC using a process very similar to those developed to optimize CIGS devices [22, 23] as has been described above. Devices for this study contained CIAS absorber layers with Al fractions from $x = 0.13$ to 0.48. The device performance parameters were obtained at IEC for all devices, and ranged from 13% to 7%, with device efficiency decreasing as the Al content of the absorber layer increased. The details of the film parameters and device properties were given above in Table II.

Sub-band-gap optical spectra of the film properties within the devices were obtained from transient photocapacitance (TPC) spectroscopy. A comparison of the lowest fraction (13at.%) Al CIAS sample device with a 27at.% Ga CIGS sample device is displayed in Fig. 16. Both of these alloys had similar bandgaps and the devices had nearly identical cell performance parameters. The fact that their photocapacitance spectra are also nearly identical gives some credence to the relevance of the TPC characterization method toward understanding how the corresponding devices are likely to behave.

The TPC spectra for all four of the CIAS devices studied are shown in Fig. 17. Here we see that the electronic properties of these alloys changes quite dramatically once the Al fraction exceeds 20at.%. Specifically, the Urbach energies (band tail widths) become much broader, indicating a much larger degree of alloy disorder[16]. The characteristic shape of the defect band "shoulder" also appears significantly flatter for the higher Al fraction alloys. We also note that the band tail extends over fewer orders of magnitude in the devices with the lowest Al fraction and believe this is likely a result of better minority carrier collection in the lower aluminum fraction devices.

FIG. 16. Comparison of Photo-capacitance Spectra for a 13at.% Al fraction CIAS device with a 27at.% Ga fraction CIGS device. Both of these devices were fabricated at IEC and were found to have nearly identical bandgaps device performance. The electronic properties indicated from these photocapacitance spectra are also nearly identical: similar defect band magnitudes and energy distributions, identical Urbach energies (17meV), and nearly identical minority carrier collection.
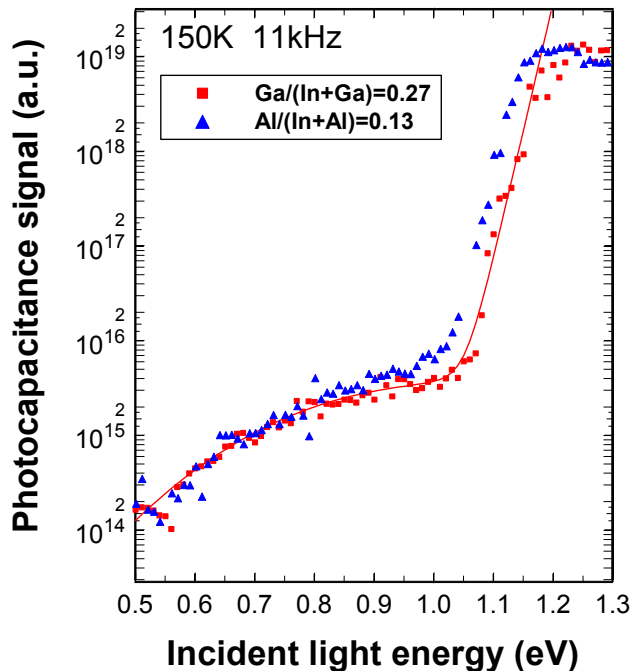
FIG. 17. Photocapacitance spectra for four CIAS samples with different Al fractions at 200 K and 11 kHz. The labels indicate Al/(In+Al) alloy fractions. Note that there is a marked increase in the Urbach energies as Al content increases beyond 20at.%. Also note the presence of the broad, featureless defect band. The smaller dynamic range of the bandtail for the 0.13 Al fraction film is probably due a higher minority carrier collection efficiency.
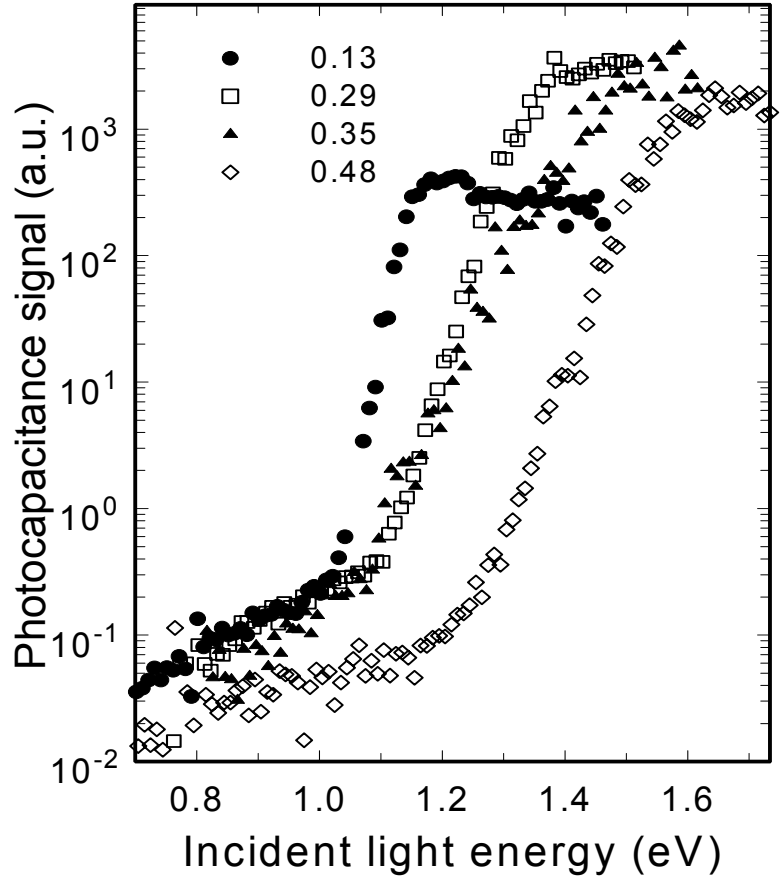
The electronic properties of these samples as deduced from these photocapacitance spectra are listed in Table V along with their device performance parameters. The broader Urbach energies probably account in part for the decrease in device open circuit voltage [24].

Admittance spectroscopy (capacitance vs. frequency) reveals a distinct step due to a dominant hole trap (deep acceptor). From an Arrhenius plot of the positions of these steps, a characteristic activation energy for this hole trap can be obtained. This response is considerable deeper in the high Al content devices, around 0.4-0.5 eV, compared to CIGS devices. However, in the device with x=0.13, the thermal response has a shallower activation energy, 0.21 eV, much more similar to that observed in CIGS. These results are also included in Table V.

Table V. Summary of device performance and defect response of CIAS samples.

Al/(In+Al)	E_G (eV)	V_{OC} (V)	J_{SC} (mA/cm^2)	FF (%)	Eff. (%)	E_U (meV)	v_0 (s^{-1}K^{-2})	E_a (eV)
0.13	1.15	0.59	34.2	65	13.1	17	1.5×10^6	0.21
0.29	1.36	0.71	25.3	63	11.3	27	1.2×10^9	0.50
0.35	1.45	0.72	21	64	9.6	42	1.5×10^9	0.45
0.48	1.67	0.72	16.9	63	6.3	35	2×10^6	0.34
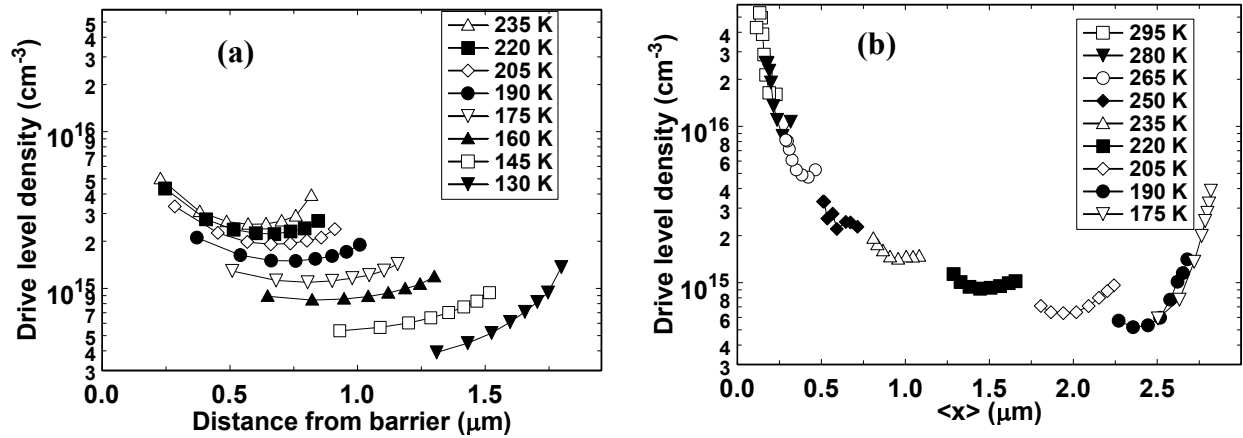
FIG. 18. DLCP data taken with f = 30 kHz, showing the spatial non-uniformity of the films, and a very low carrier density. **(a)** Results for the device with Al/(In+Al) = 0.13 **(b)** Results for the device with Al/(In+Al) = 0.35. These are characteristic of all devices with Al/(In+Al) ≥ 0.2.

DLCP measurements were also carried out on this set of CIAS films and the most uniform DLC profiles were obtained for the device with x = 0.13. These profiles are displayed in Fig. 18(a); however, even these were found to be significantly less uniform than those obtained in typical IEC CIGS based devices. Moreover, the results for the CIAS devices with higher Al content are quite dramatically non-uniform, as illustrated for one sample in Fig. 18(b).

To better understand the very non-uniform DLCP results on the higher Al fraction samples, we have simulated this measurement using a numerical solution of Poisson's equation. More details of how we carry out this modeling have been described in Section 3.4 above. This
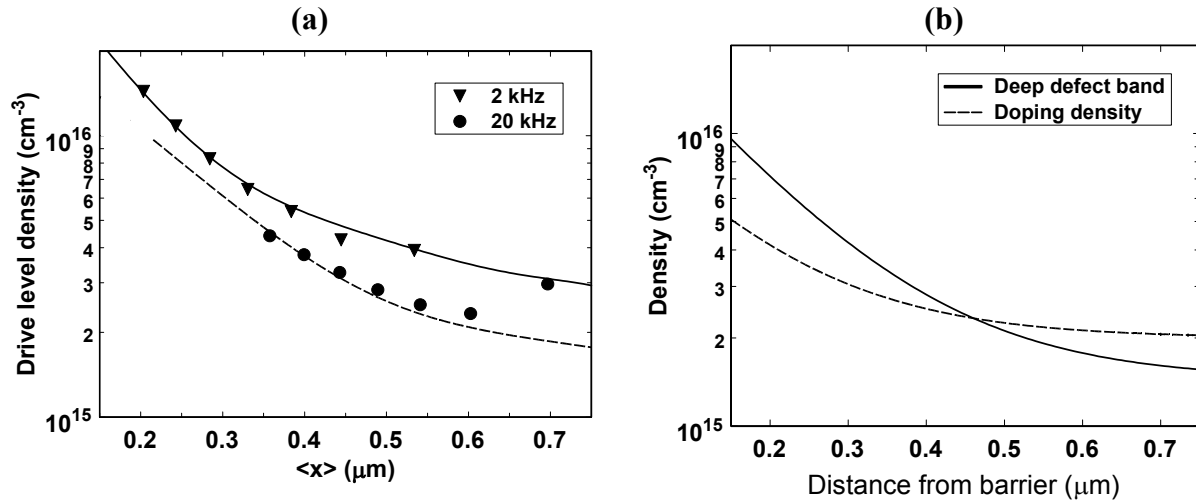
FIG. 19. (a) Solid symbols are DLCP data for device with Al/(In+Al) = 0.29, taken at 270 K and frequencies of 2 kHz (triangles) and 20 kHz (circles). Lines show numerically simulated results. **(b)** Illustration of the simulation parameters used to generate the experimental data of (a). The model assumes a deep defect band 0.5eV above E_V, with width 0.025 eV (solid line), and magnitude exponentially decreasing with distance from the barrier. The doping density (dotted line) also decreases exponentially with distance, with the same decay length (0.14 μm).

modeling indicates that both a strongly non-uniform carrier density as well as a non-uniform defect density distribution must be present to account for the observed DLCP results in these CIAS devices. The best fit we have found to account for these data requires an exponential dependence of both the carrier density and deep defect density, with these values increasing rapidly near the junction. Experimental data and the best fit for the device with $x = 0.29$ are illustrated in Fig. 19.

These experimental data thus again indicate a sharp difference between our devices with lower Al content and those with $x \geq 0.2$. The results for the device with $x = 0.13$, which has an activated response around $E_a = 0.21$ eV with a relatively uniform density through the film, and a sharp band edge with $E_U < 20$ meV, are similar to our observations of good quality $CuInSe_2$ and CIGS devices. The broader band edge and the spatially non-uniform, deeper thermal response in the higher Al content devices is indicative of poorer electronic properties in these films. Our initial assessment of this latter result is that the effective doping density becomes much lower and much less uniform for the higher Al fraction samples.

## 3.7 Modulated Elemental Film Synthesis of CGS and CIS Films

Initial investigation demonstrated the formation of a kinetically assessable amorphous phase near the composition Cu:Se 1:2 for modulated elemental reactants with layer thicknesses under 100 Å. For the In-Se system, kinetically stable amorphous alloys were observed near the composition In:Se 1:1. The low angle diffraction patterns did not show any elemental layering on deposit. During this initial phase of the project, we confirmed the cross deposition of selenium during Cu and In deposition and demonstrated the unwanted effects on composition control and the uniformity of deposited films. Several methods were used to eliminate cross deposition and we were finally able to eliminate this problem. During recalibration, outstanding low angle diffraction patterns of binary In-Se modulated elemental reactants were observed when previously we did not observe the expected Bragg diffraction maxima in this system. Recalibrating the Cu-Se binary system we observed again observed the formation of a kinetically stable amorphous phase near the composition Cu:Se 1:2. At the 1:1 composition, CuSe was observed to nucleate. If thick layers of Cu and Se were deposited (greater than 100Å repeats), CuSe was observed to nucleate at the reacting interfaces over the entire composition range investigated.

During our initial attempts to deposit micron thick films to make devices for testing, we observed significant drift in the deposition rates of the In and Se. To better define the problem with deposition consistency when using our old cells, we deposited five sequential samples of copper-indium-selenium with the same layer thicknesses and desired composition. Each sample was 2000 angstroms thick which with the five depositions combined adds up to one micron, the thickness of the sample we intend to eventually deposit. Figure 20 shows the relative composition of the five samples as determined by electron probe microanalysis. A variation of 15% in elemental composition through the sample is unacceptable.

After several attempts at modifying our home-built effusion sources, we decided to upgrade the sources, purchasing a set of precision effusion cells from Applied Epi. These cells are designed to maintain a constant temperature around a crucible filled with the element being deposited. Precise control of temperature leads to a consistent emission of elemental flux

FIG. 20. Composition vs. deposition time of five sequentially deposited samples relative to Se_2
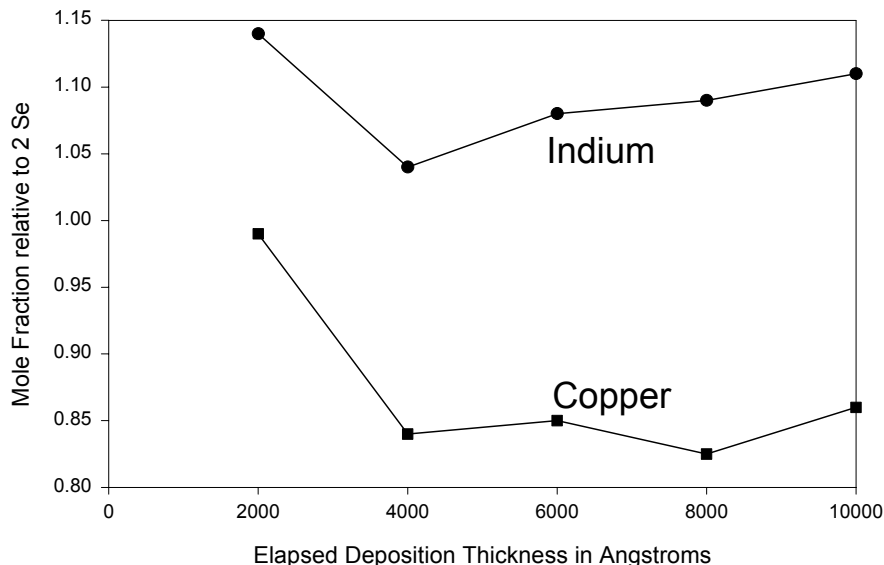
eliminating the need for flux monitoring. Our method of flux monitoring using quartz crystal monitors is not compatible with the deposition of indium or gallium. Gallium turns to a liquid at just above room temperature confusing the crystal monitor and indium creates a non-linear response in the crystal when small amounts of selenium are present (which is unavoidable when making CIS or CGS). A set of test superlattices were prepared using the new cells and compared to a similar set of superlattices prepared with the old deposition sources. The old method produced samples with layer thicknesses ranging from 77.5 to 82.2 angstroms with a standard deviation of 1.97 angstroms. The new cells produced samples with layer thicknesses ranging from 81.3 to 81.5 angstroms with a standard deviation of 0.054 angstroms. This indicates a massive improvement in the control of the deposition rates. Although the elements are different, we anticipate an equivalent improvement in accuracy over long deposition times. The consistency of composition has been established by the sequential deposition of three samples, each 2000 angstroms thick onto separate substrates. Figure 21 displays the composition data from electron microprobe analysis of the thin film samples on silicon. This same improvement in consistency was observed in parallel experiments on CGS samples as well.
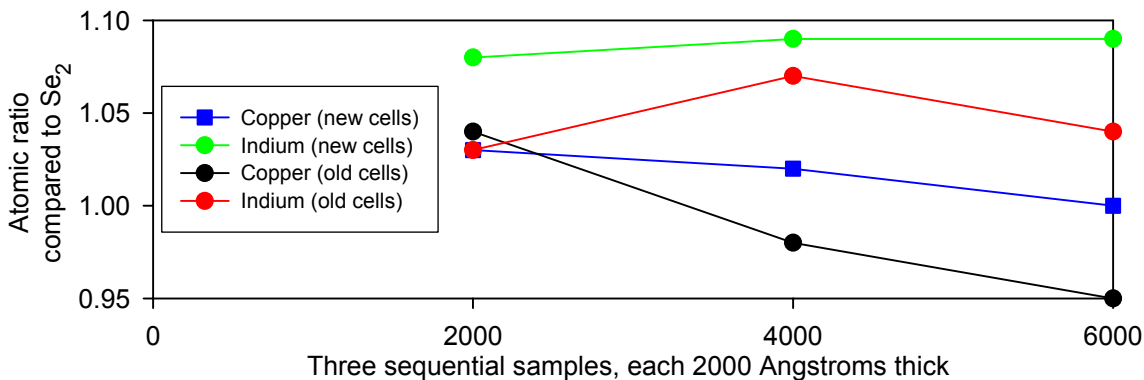

FIG. 21. Composition of three sequentially deposited samples of CIS.
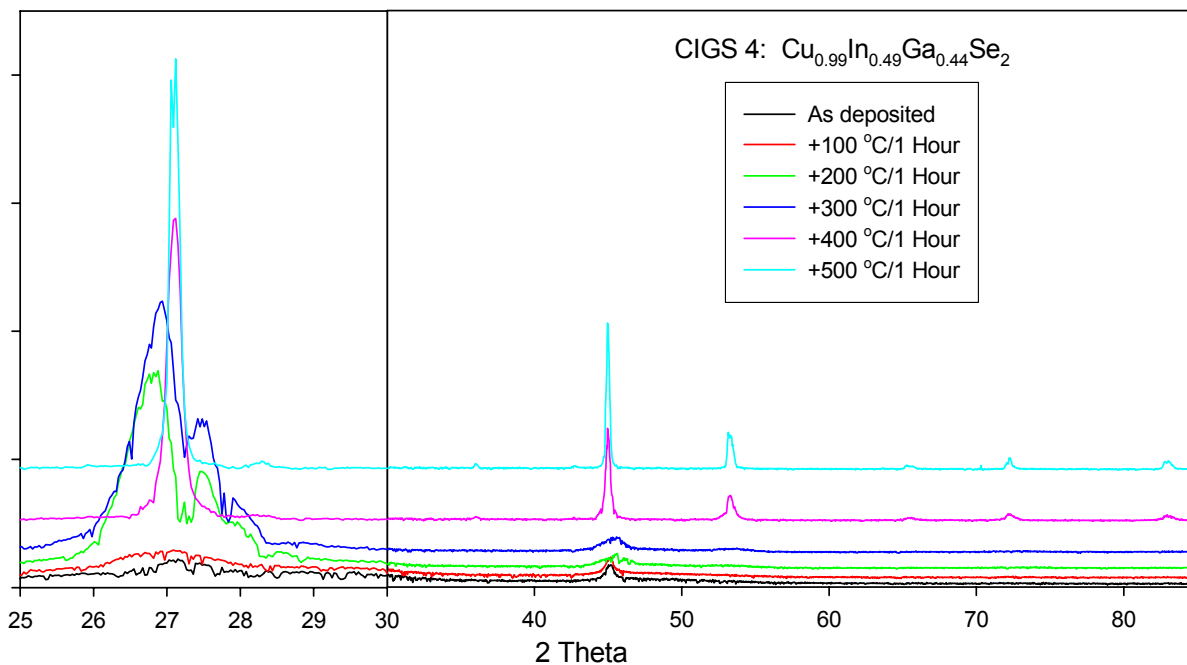
24

FIG. 22. X-ray diffraction for a series of anneals of a (Cu:In:Se)/(Cu:Ga:Se) layered composite. The layers were 100Å thick and there were 50 repetition each of the In containing and the Ga containing layers. The higher angle data for this sample after the 200 ºC and 300 ºC anneals shows two distinct (112) peaks, one for CIS with some gallium and one for CGS with some indium. Note that after the 400 ºC anneal, the two layers have interdiffused and only a single (112) peak is observed.

Using the new effusion cells, multiple samples of CIS, CGS, and CIGS were deposited, annealed at multiple temperatures between 100 ºC and 500 ºC, and analyzed by x-ray diffraction to follow the crystallization of the material. Generally, the as-deposited samples are nanocrystalline and the crystallites grow as the temperature is increased. The rate of growth of the crystallites varies with the composition and the annealing temperature at which rapid crystallite growth occurs also varies with composition.

One sample of specific interest is composed of 50 repetitions of 100 angstroms of thin Cu:In:Se layers followed by 100 angstroms of thin Cu:Ga:Se layers. Figure 22 follows the crystallinity of the sample after annealings up to 500 ºC. Although x-ray reflectivity data (not shown) does not indicate the existence of two distinct layers, the high angle data for the sample after the 200 ºC and 300 ºC anneals shows two distinct (112) peaks, one for CIS with some gallium and one for CGS with some indium. After the 400 ºC anneal, the two layers have interdiffused and only a single (112) peak is observed. This suggests that samples with graded composition profiles will have their composition gradients reduced on annealing at temperatures above 400°C.

Several additional samples have been deposited on molybdenum coated glass provided by Bill Shafarman, at IEC, University of Delaware. He agreed to add CdS and ZnO layers on top of our films to produce completed solar cells. Their performance parameters will be determined at Delaware, and then they will be returned to Oregon for additional testing of their electronic

properties by the Cohen lab. Approximately 10 samples were sent to be coated at IEC for us. While we are still awaiting the return of these samples for testing by the Cohen laboratory, preliminary tests at IEC reveal that the best of these samples produced a 2.5% efficient cell. Since we have found diffraction data for different samples and different annealing conditions to be indistinguishable, electrical tests will be required to determine the origin of the performance differences between films.

4.0 SUMMARY AND CONCLUSIONS

Although the initial emphasis of the work supported under this NREL Subcontract was on the synthesis of CIGS materials by our modulated elemental deposition techniques, this shifted as the Subcontract period progressed due to the increasing success demonstrated by our efforts to characterize the electronic properties of such CIGS materials. This was accomplished by utilizing a variety of capacitance spectroscopic methods. In the near future such methods will be applied to the CIGS material being developed here. However, all of the characterization work described in this report was carried out on state-of-the-art CIGS samples obtained from several outside laboratories, particularly from the Institute of Energy Conversion at the University of Delaware. Because these outside samples represent some of the best laboratory photovoltaic cells currently available, our characterization of these CIGS absorber layers has provided an important baseline that, in the near future, we will use to assess CIGS material that is being synthesized at Oregon.

Key accomplishments of the work carried out under this Subcontract include, first of all, the application of transient photocapacitance (TPC) spectroscopy to identify the sub-band-gap optical transitions from defects in CIGS materials. Two types of transitions were identified: a deep defect band centered about 0.8 eV from the top of the valence band, and an exponential tail of states extending (most likely) from the bottom of the conduction band into the gap. The deep defect band was found to be present both in the polycrystalline CIGS samples from IEC, as well as a single crystal epitaxial sample device provided by Angus Rockett at the University of Illinois. Thus, we concluded this defect was *not* associated with grain boundaries but was likely a point defect in the CIGS crystal lattice itself. Moreover, the 0.8 eV optical transition energy remained constant, independent of changes in the bandgap energy, as the Ga fraction was varied from 0 to 80at.%. This implies that the energy of this defect likely lies much closer to midgap for the higher Ga fractionalloys. Thus, it is also likely that this defect functions as a more important recombination center in the higher Ga fraction alloys.

Second, we characterized a series of 30at.% Ga fraction samples devices supplied by IEC that exhibited a range of conversion efficiencies. Our photocapacitance spectra exhibited distinct differences as well. We found that the poorer efficiency devices had lower minority carrier collection fractions which we determined by comparing photocapacitance with transient photocurrent spectroscopy. We also found that for the samples with higher Urbach energies, indicating higher alloy disorder, the short-circuit current was lower. In addition, both the TPC measurements and admittance measurements indicated additional defect bands in the material that had been deposited at lower temperatures.

Third, we demonstrated the utility of the drive-level capacitance profiling (DLCP) method to the study of these materials. We argued that such measurements provided superior quantitative estimates of the deep majority carrier trap (the "deep acceptor level") and, perhaps, the first

reliable estimates of the hole carrier densities in sandwich geometry CIGS devices. Numerical modeling studies were employed to confirm these conclusions, and to point out the detailed relationship and significant differences between the DLCP method with the more familiar admittance spectroscopy, or standard capacitance-voltage profiling.

Fourth, we extended our characterization studies to four $CuIn_{1-x}Al_xSe_2$ (CIAS) samples supplied by IEC. It had been hoped that, because a much smaller fraction of Al is needed to increase the bandgap of these copper based chalopyrite materials than through substitution by Ga, that Al alloying might lead to bandgaps larger than 1.4eV without the deterioration in device performance observed with higher levels of Ga alloying. Our photocapacitance and DLCP on the CIAS samples indicated that, for the sample with 13at.% Al (and a bandgap near 1.2eV) the electronic properties were essentially identical to those in CIGS samples with 26at.% Ga. However, for the CIAS samples with 29at.% and higher Al fractions the electronic properties were found to be poor, as indicated by broader bandtails, poorer minority carrier collection, very nonuniform electronic properties, and generally lower carrier densities.

Finally, we were able to demonstrate the ability to prepare CIS samples from modulated elemental reactants at temperatures below 400°C. The best of the samples we produced only had an efficiency of 2.5%, however, we hope that further and more rapid improvement will be possible once we have carried out a detailed characterization of their electronic properties. The ability to prepare CIS at these low temperatures, if the efficiency could be raised, provides an opportunity to use cheaper substrates (e.g., polymers) for substrates, potentially reducing the cost of solar modules.

5.0 SUBCONTRACT SUPPORTED PUBLICATIONS

1. J.T. Heath, J.D. Cohen, W.N. Shafarman, and D.C. Johnson, "Characterization of deep defects in $CuIn_{1-x}Ga_xSe_2$ (CIGS) working photovoltaic devices", in *Photovoltaics for the 21st Century*, ed. by V. K. Kapur, R. D. McConnell, D. Carlson, G. P. Caesar, A. Rohatgi, and J. Smith (Electrochem. Soc. Conf. Proc., 2001), Vol. **2001-10**, pp.324-332.

2. J. O. Thompson and D. C. Johnson, "Synthesis and Characterization of CuInSe2, CuGaSe2 and Graded Compositions from Modulated Elemental Reactants", in *Photovoltaics for the 21st Century*, ed. by V. K. Kapur, R. D. McConnell, D. Carlson, G. P. Caesar, A. Rohatgi, and J. Smith (Electrochem. Soc. Conf. Proc., 2001), Vol. **2001-10**, pp.317-323

3. J.T. Heath, J.D. Cohen, W.N. Shafarman, D.X. Liao and A.A. Rockett, "Effect of Ga content on defect states in $CuIn_{1-X}Ga_XSe_2$ photovoltaic devices" Appl. Phys. Lett. **80**, 4540 (2002).

4. Jennifer Heath, J. David Cohen, and William N. Shafarman, "Correlation between deep defect states and device parameters in $CuIn_{1-X}Ga_XSe_2$ photovoltaic devices**",** Proc. of the 29th IEEE Photovoltaic Specialists Conference - 2002, 204.4 (2002).

5. J.T. Heath, J.D. Cohen, and W.N. Shafarman, "Distinguishing metastable changes in bulk CIGS defect densities from interface effects", Thin Solid Films **431-432**, 426 (2003).

6. J. David Cohen, Jennifer Heath, and William N. Shafarman, "New junction capacitance methods for the study of defect distributions and carrier properties in the copper indium diselenide alloys**",** Mat. Res. Soc. Symp. Proc. **763**, 429 (2003).

7. Jennifer Heath, J. David Cohen, and William N. Shafarman, "Defects in copper indium aluminum diselenide films and their impact on photovoltaic device performance**",** Mat. Res. Soc. Symp. Proc. **763**, 441 (2003).

8. J.T. Heath, J.D. Cohen, and W.N. Shafarman, "The study of bulk and metastable defects in $CuIn_{1-X}Ga_XSe_2$ thin films using drive-level capacitance profiling", J. Appl. Phys., in press.

6.0 REFERENCES AND BIBLIOGRAPHY

1. Lang, D. V.; Cohen, J. D.; Harbison, J. P. *Phys. Rev. B* **1982**, *25*, 5285.

2. Goodman, A. M. *J. Appl. Phys.* **1963**, *34*, 329.

3. Lang, D. V.; Cohen, J. D.; Harbison, J. P. *Phys. Rev. B* **1982**, *25*, 5285.

4. Cohen, J. D.; Lang, D. V. *Phys. Rev. B* **1982**, *25*, 5321.

5. Michelson, C. E.; Gelatos, A. V.; Cohen, J. D. *Appl. Phys. Lett.* **1985**, *47*, 412.

6. Gelatos, A. V.; Cohen, J. D.; Harbison, J. P. *Appl. Phys. Lett.* **1986**, *49*, 722.

7. Essick, J. M.; Cohen, J. D. *Appl. Phys. Lett.* **1989**, *55*, 1232.

8. Fister, L.; Li, X. M.; Novet, T.; McConnell, J.; Johnson, D. C. *J. Vac. Sci. & Technol. A* **1993**, *11*, 3014–3019.

9 . Novet, T.; Johnson, D. C. *J. Am. Chem. Soc.* **1991**, *113*, 3398–3403.

10. Novet, T.; Johnson, D. C.; Fister, L. In *Materials Chemistry, An Emerging Discipline*; L. V. Interrante, L. A. Casper and A. B. Ellis, Ed.; American Chemical Society: Washington, DC, 1995; Vol. 245; pp 425-470.

11. Novet, T.; McConnell, J. M.; Johnson, D. C. *Chemistry of Materials* **1992**, *4*, 473-478.

12. Novet, T.; McConnell, J. M.; Johnson, D. C. *Materials Research Society* **1992**, *238*, 581-586.

13. Novet, T.; Xu, Z.; Kevan, S. D.; Johnson, D. C. *Materials Science and Engineering A: Structural Materials: Properties, Microstructure and Processing* **1992**, *A 162*, 115.

14. W. N. Shafarman, R. Klenk, B. E. McCandless, J. Appl Phys. **79** (1996) 7324.

15. W. N. Shafarman, J. Zhu, Mat. Res Soc. Symp. Proc. **668** (2001) H2.3.

16. S. M. Wasim, C. Rincón, G. Marín, P. Bocaranda, E. Hernández, I. Bonalde, and E. Medina, Phys. Rev. B **64**, 195101 (2001).

17. S.H. Wei, S.B. Zhang, and A. Zunger, Appl. Phys. Lett. **72**, 3199 (1998).

18. U. Rau, K. Weinert, Q. Nguyet, M. Mamor, G. Hanna, A. Jasenek, H. W. Schock Mat. Res. Symp. Proc. **668**, H9.1 (2001).

19. R. Herberholz, M. Igalson, and H. W. Schock, J. Appl. Phys. **83**, 318 (1998).

20. T. Unold, J. Hautala, and J.D. Cohen, Phys. Rev. B**50**, 16985 (1994).

21. U. Rau, D. Braunger, R. Herberholz, H. W. Schock, J. –F. Guillemoles, L. Kronik, and D. Cahen, J. Appl. Phys. 86, 497 (1999).

22. W. N. Shafarman, S. Marsillac, P. D. Paulson, M. W. Haimbodi, T. Minemoto, and R. W. Birkmire, in *Proceedings of the 29th IEEE PVSC*, 519 (2002).

23. W. N. Shafarman, R. Klenk, and B. E. McCandless, J. Appl. Phys. **79**, 7324 (1996).

24. T. Tiedje, Appl. Phys. Lett. **40**, 627 (1982).

REPORT DOCUMENTATION PAGE			*Form Approved* *OMB NO. 0704-0188*

Public reporting burden for this collection of information is estimated to average 1 hour per response, including the time for reviewing instructions, searching existing data sources, gathering and maintaining the data needed, and completing and reviewing the collection of information. Send comments regarding this burden estimate or any other aspect of this collection of information, including suggestions for reducing this burden, to Washington Headquarters Services, Directorate for Information Operations and Reports, 1215 Jefferson Davis Highway, Suite 1204, Arlington, VA 22202-4302, and to the Office of Management and Budget, Paperwork Reduction Project (0704-0188), Washington, DC 20503.

1. AGENCY USE ONLY (Leave blank)	2. REPORT DATE May 2004	3. REPORT TYPE AND DATES COVERED Final Subcontract Report 1 July 1999–31 August 2003	
4. TITLE AND SUBTITLE Novel Capacitance Measurements in Copper Indium Gallium Diselenide Alloys: Final Subcontract Report, 1 July 1999–31 August 2003			5. FUNDING NUMBERS PVP42100 XAD-9-18668-15
6. AUTHOR: D.C. Johnson			
7. PERFORMING ORGANIZATION NAME(S) AND ADDRESS(ES) Department of Chemistry and Materials Science Institute University of Oregon Eugene, Oregon 97403-5219			8. PERFORMING ORGANIZATION REPORT NUMBER
9. SPONSORING/MONITORING AGENCY NAME(S) AND ADDRESS(ES) National Renewable Energy Laboratory 1617 Cole Blvd. Golden, CO 80401-3393			10. SPONSORING/MONITORING AGENCY REPORT NUMBER NREL/SR-520-35614
11. SUPPLEMENTARY NOTES NREL Technical Monitor: R. Matson			
12a. DISTRIBUTION/AVAILABILITY STATEMENT National Technical Information Service U.S. Department of Commerce 5285 Port Royal Road Springfield, VA 22161			12b. DISTRIBUTION CODE

13. ABSTRACT (Maximum 200 words):

This subcontract report describes the University of Oregon's objectives to measure the electronic properties of the copper indium/gallium diselenide alloys using several well-developed capacitance techniques appropriate for probing materials with a continuous distribution of semiconducting gap electronic energy states. We applied a new synthetic method to the production of CIGS alloys, namely, the modulated elemental reactant method. To form CIGS by this method, alternating layers of Cu:In:Se and Cu:Ga:Se composites, each less than 100 Å thick, were evaporated in sequence and then annealed at low temperature. A second focus was to test and develop junction capacitance methods to better understand the electronic properties in CIGS material and establish a relationship of those properties to specific device performance parameters. The primary methods employed were transient photocapacitance (TPC) spectroscopy and drive-level capacitance profiling (DLCP). Finally, we extended our characterization studies to four $CuIn_{1-x}Al_xSe_2$ (CIAS) samples, also supplied by IEC. Our photocapacitance and DLCP measurements on these CIAS samples indicated that for a sample with 13 at.% Al (having a bandgap of nearly 1.2 eV), the electronic properties were essentially identical to those in CIGS samples with 26 at.% Ga.

14. SUBJECT TERMS: PV; thin film; solar cell; modulated elemental reactant method; junction capacitance; electronic properties; device; transient photocapacitance (TPC); drive-level capacitance profiling (DLCP); bandgap; copper indium; gallium diselenide			15. NUMBER OF PAGES
			16. PRICE CODE
17. SECURITY CLASSIFICATION OF REPORT Unclassified	18. SECURITY CLASSIFICATION OF THIS PAGE Unclassified	19. SECURITY CLASSIFICATION OF ABSTRACT Unclassified	20. LIMITATION OF ABSTRACT UL